

Supplementary Information

Achieving High-Efficient Carbon Radical-Mediated Cross-Coupling Reaction by Confined Radical Microenvironment in Metal-Organic Framework

Ying-Lin Li,^a Ning Li,^{*,a} Zhi-Bin Mei,^a Jun-Rong Li,^a Su-Juan Yao,^a Fei Yu,^b Shun-Li Li,^a Jiao-Min Lin,^{*,a} Jiang Liu,^{*,a} and Ya-Qian Lan^a

^a *National and Local Joint Engineering Research Center of MPTES in High Energy and Safety LIBs, Engineering Research Center of MTEES (Ministry of Education), and Key Lab. of ETESPG (GHEI), School of Chemistry, South China Normal University, Guangzhou, 510006, China.*

^b *Jiangsu Collaborative Innovation Centre of Biomedical Functional Materials, Jiangsu Key Laboratory of New Power Batteries, School of Chemistry and Materials Science, Nanjing Normal University, Nanjing, 210023, China.*

E-mail: ningl0314@163.com; linjm@m.scnu.edu.cn; liuj0828@m.scnu.edu.cn.

Homepage: <http://www.yqlangroup.com>

Materials and General Methods

Materials.

All materials, reagents and solvents used in experiments were commercially available, high-grade purity materials, and used without further purification. 2,7-dihydroxybenzo[*lmn*][3,8]phenanthroline-1,3,6,8(2H,7H)-tetraone (97%) were purchased from Jilin Chinese Academy of Sciences-Yanshen Technology Corporation LTD. Zirconyl dichloride oxide octahydrate ($\text{ZrOCl}_2 \cdot 8\text{H}_2\text{O}$) and hafnium dichloride oxide octahydrate ($\text{HfOCl}_2 \cdot 8\text{H}_2\text{O}$) were purchased from Shanghai Macklin Biochemical Corporation LTD. N, N-dimethylformamide (DMF), ethanol (EtOH), formic acid (HCOOH), triethylamine (TEA), *o*-phenylenediamine (OPD) were purchased from Shanghai Adamas Reagent Corporation LTD. All aqueous solutions were prepared using deionized water (18.25 M Ω).

Instruments.

The Powder X-ray diffraction (PXRD) spectra of the materials were recorded on a Rigaku SmartLab diffractometer (Japan) equipped with Cu K α ($k=1.54060 \text{ \AA}$) radiation at 40 kV and 200 mA. Fourier transform infrared spectroscopy (FTIR) was recorded on a Nicolet iS50 Fourier transform infrared spectrometer (Thermo Scientific, USA) in the range of 4000-400 cm^{-1} using the technique of pressed KBr pellets. The solid-state ultraviolet-visible (UV-vis) absorption spectroscopy were acquired on a Cary 5000 (Varian, USA) in the wavelength range of 200-2500 nm. Thermogravimetric analysis (TGA) was carried out on a STA449F3 analyzer (Netzsch, Germany) under the ambient atmosphere heated from room temperature to 800 °C at 10 °C/min. Electron paramagnetic resonance (EPR) experiments were conducted on EMX PLUS (Bruker, Germany). The electrochemical tests were carried out with an EC-Lab SP-150 workstation (Bio-Logic, France). The catalytic liquid products were analyzed by gas chromatography-mass spectrometer (GC-MS) (Agilent 7890B and 5977B equipped HP-5-MSUI or HP-PLOT Molesieve capillary column, USA). The gaseous products of photocatalysis were monitored by gas chromatography (GC-7920A, Aulight Co.) equipped with a flame ionization detector (FID) with methanizer and a thermal conductivity detector (TCD). The high-resolution mass spectrometry (HRMS) of the radical-adduct was carried on Thermo Scientific Q Exactive. Single-crystal XRD data of crystals were measured on an APEXII CCD diffractometer (Bruker, Germany) with graphite-monochromated Mo K α radiation ($k=0.71073 \text{ \AA}$) at 296 K. All the structures were solved by direct method using SHELXT program and refined on an Olex2 software. The detailed crystallographic information of crystals is listed in Table S1. The Cambridge Crystallographic Data Centre (CCDC) numbers of **Zr-NDI** and **Hf-NDI** were 2351583 and 2351584. Nitrogen sorption was measured at 77.3 K using an Autosorb IQ2 absorptiometer (Quantachrome Instruments) volumetric adsorption analyzer. Apparent surface areas were determined using the BET method.

Experimental Procedures

Synthesis of Zr-NDI.

0.01 mmol of $\text{ZrOCl}_2 \cdot 8\text{H}_2\text{O}$ and 0.01 mmol of H_2NDI were dispersed in 0.6 mL of N, N-dimethylformamide (DMF) solution, and the mixture was stirred for about 10 minutes. Then 0.3 mL of HCOOH was slowly added dropwise to the above mixture. Subsequently, the mixture solution

was transferred into a 10 mL glass vial and heated at 120 °C for 72 h. After cooling down to room temperature, red single crystals of **Zr-NDI** were collected, and washed with CH₃CN. (Yield: about 68 %)

Synthesis of Hf-NDI.

0.01 mmol of HfOCl₂·8H₂O and 0.01 mmol of H₂NDI were dispersed in 0.6 mL of N, N-dimethylformamide (DMF) solution, and the mixture was stirred for about 10 minutes. Then 0.3 mL of HCOOH was slowly added dropwise to the above mixture. Subsequently, the mixture solution was transferred into a 10 mL glass vial and heated at 120 °C for 72 h. After cooling down to room temperature, red single crystals of **Hf-NDI** were collected, and washed with CH₃CN. (Yield: about 65 %)

Amine induced radical MOFs formation.

At room temperature, 5 mL of triethylamine, ammonia, ethylamine and ethylenediamine was added to the vessel respectively, and the **Zr-NDI/Hf-NDI** samples were hollowed out in it, finally sealed it and made sure they were in the same enclosed space. These amine were extremely easy to gasify into vapor, and can be able to enter into MOFs channels. After a certain period of time, the color of the crystals gradually changed from red to black, as shown in Figure S18-S22.

Photocatalytic experiments.

0.05 mmol of OPD, 10 mg of catalyst and 10 mL of ethanol were added to a sealed quartz reactor. Before reaction, the suspension was purged with argon for 30 min. Afterward, a 300 W xenon arc lamp with a wavelength range from 250 to 1100 nm was used as light source to trigger the photocatalytic reaction. The reaction temperature was controlled at 298 K by using the cooling cycle water. After 12 hours of reaction, the gaseous products were detected by gas chromatograph (GC-7920A, Aulight Co.,) and the liquid products were monitored by gas chromatography–mass spectroscopy (GC-MS) and quantified by GC.

Photoelectrochemical measurements.

The Photoelectrochemical measurements of photocurrent, Mott-Schottky and electrochemical impedance (EIS) were carried out on the electrochemical workstation (CHI 660e) with a standard three-electrode system. The as-synthesized crystal power (2 mg) was added into 1 mL solution (990 μL ethanol and 10 μL 0.5 % Nafion) and ultrasound for 30 min to form the mixture. Then, 200 μL of the mixture were dropping onto the surface of ITO glass substrate and dried at room temperature as the working electrodes. Pt plate as the counter electrode, Ag/AgCl electrode as the reference electrode and 0.5 M Na₂SO₄ aqueous solution as the electrolyte. Photocurrent tests were carried out under Xe lamp as the light source. The Mott-Schottky plots were measured at the frequencies of 500, 1000 and 1500 Hz.

Theoretical calculations.

Density functional theory (DFT) calculations were performed to deeply understand the catalyst's function and the detailed reaction mechanisms. DFT calculations were calculated using CP2K code (freely available at <http://www.cp2k.org>)¹, based on the mixed Gaussian and plane-wave scheme² and the Quickstep module.³ The calculation used molecularly optimized Double-Zeta-

Valence plus Polarization (DZVP) basis set,⁴ Goedecker-Teter-Hutter pseudopotentials,⁵ and the Perdew-Burke-Ernzerhof (PBE)⁶ exchange correlation functional with the D3 dispersion corrections proposed by Grimme.⁷ The plane-wave energy cutoff was 400 Ry. The calculation was performed on Gamma point only, with no symmetry constraint. Structural optimization was performed using the Broyden-Fletcher-Goldfarb-Shannon (BFGS) optimizer, until the maximum force is below 0.00045 Ry/Bohr (0.011 eV/Å). The cluster/adsorbate systems were modelled within the repeated Scheme, 30 Ångstroms of vacuum were included in the simulation cell to decouple the system from its periodic replicas in the direction perpendicular to the surface. To obtain the equilibrium geometries, we kept the atomic positions of the Zr-NDI MOF fixed based on the single crystal structures; all other atoms were relaxed until forces were lower than 0.005 eV Å⁻¹.

Table S1. Crystal data and structure refinement of **Zr-NDI** and **Hf-NDI**.

| | Zr-NDI | Hf-NDI |
|--|---|---|
| Formula | C ₃₅ H ₁₂ N ₅ O ₁₆ Zr | C ₃₈ H ₁₉ N ₆ O ₁₇ Hf _{0.99} |
| Formula weight | 849.72 | 1008.30 |
| Temperature/K | 150.00 | 150.00 |
| Crystal system | monoclinic | monoclinic |
| Space group | <i>P2₁/c</i> | <i>P2₁/c</i> |
| <i>a</i> /Å | 14.6361(14) | 14.6361(14) |
| <i>b</i> /Å | 21.520(2) | 21.520(2) |
| <i>c</i> /Å | 11.8409(13) | 11.8409(13) |
| α /° | 90 | 90 |
| β /° | 103.015(4) | 103.015(4) |
| γ /° | 90 | 90 |
| Volume/Å ³ | 3633.8(7) | 3633.8(7) |
| <i>Z</i> | 4 | 4 |
| <i>D</i> _{calc} /g cm ⁻³ | 1.552 | 1.843 |
| μ /mm ⁻¹ | 0.385 | 2.935 |
| <i>F</i> (000) | 1700.0 | 1985.0 |
| Reflections collected | 19175 | 72921 |
| Independent reflections | 6343 | 6406 |
| GOF on <i>F</i> ² | 1.039 | 1.072 |
| <i>R</i> _{int} | 0.0772 | 0.0464 |
| <i>R</i> ₁ [<i>I</i> > 2σ(<i>I</i>)] ^a | 0.0638 | 0.0258 |
| <i>wR</i> ₂ [<i>I</i> > 2σ(<i>I</i>)] ^a | 0.1576 | 0.0669 |
| <i>R</i> ₁ (all data) ^b | 0.0893 | 0.0275 |
| <i>wR</i> ₂ (all data) ^b | 0.1738 | 0.0679 |

^a $R_1 = \sum ||F_o| - |F_c|| / \sum |F_o|$, ^b $wR_2 = [\sum w(F_o^2 - F_c^2)^2 / \sum w(F_o^2)]^{1/2}$.

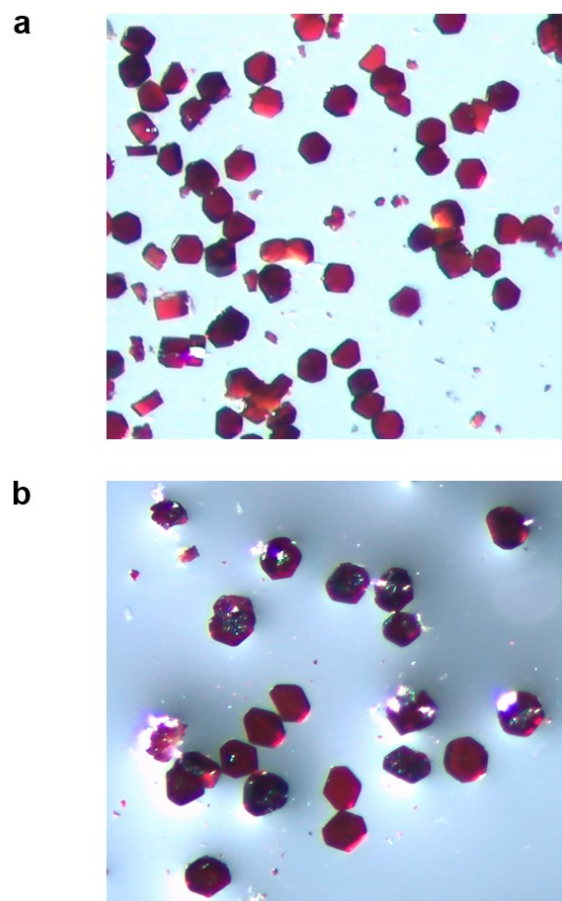


Figure S1. The images of (a) **Zr-NDI** and (b) **Hf-NDI** crystals under optical microscope.

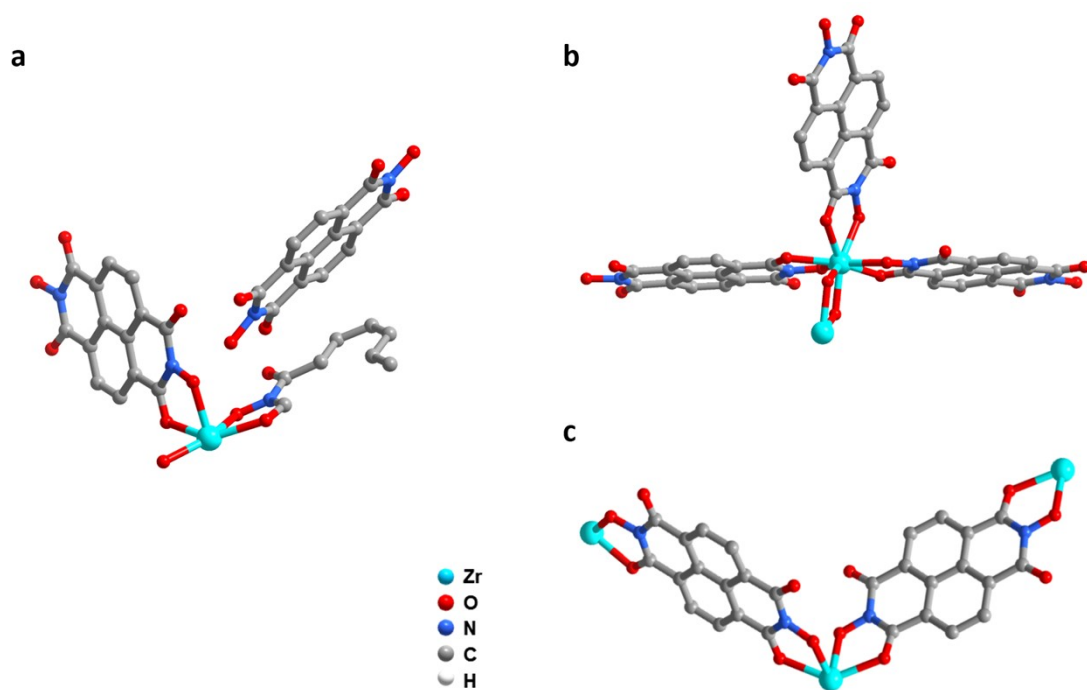


Figure S2. (a) The asymmetric unit of **Zr-NDI** contains one Zr⁴⁺ ion, 3/2 NDI²⁻ ligands, one μ_2 -OH⁻, one uncoordinated H₂NDI ligand and some disorder solvent molecules, which are difficult to model. (b) The coordination environment of the metal ion. Each Zr⁴⁺ ion was coordinated by eight O atoms, with six O atoms from three NDI²⁻ ligands and two O atoms from two μ_2 -OH⁻. Two Zr⁴⁺ ions were connected together by two μ_2 -OH⁻ to form a binuclear Zr₂ unit. (c) The coordination mode of the NDI ligand. All hydrogen atoms were omitted for clarity.

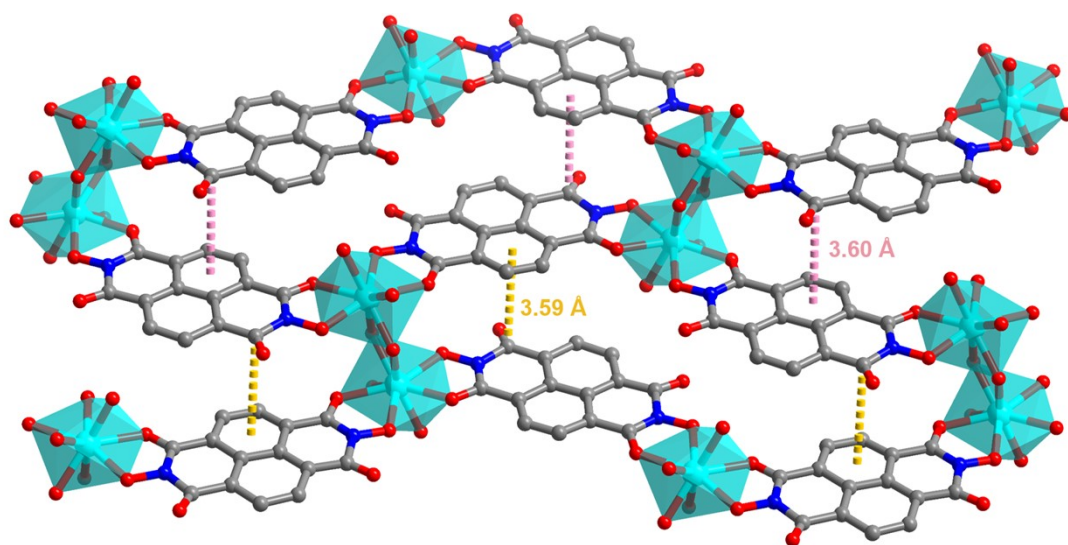


Figure S3. The expanded view of Zr-NDI along the *a*-axis.

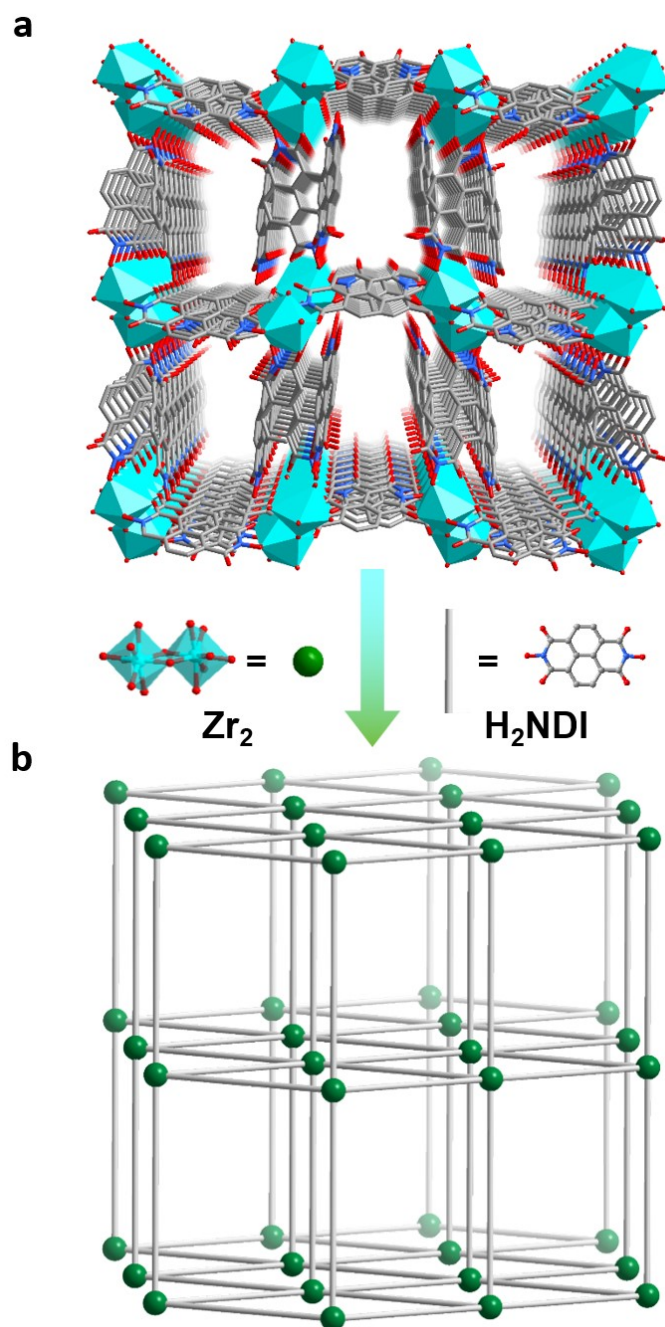


Figure S4. (a) The three-dimensional structural of **Zr-NDI**. All hydrogen atoms are omitted for clarity. Zr, lake blue, O, red, C, gray, N, blue. (b) Regarding the binuclear Zr_2 unit as a 6-connected node, and the NDI^{2-} ligand as a 2-connected linker, **Zr-NDI** can be simplified to *pcu* topology.

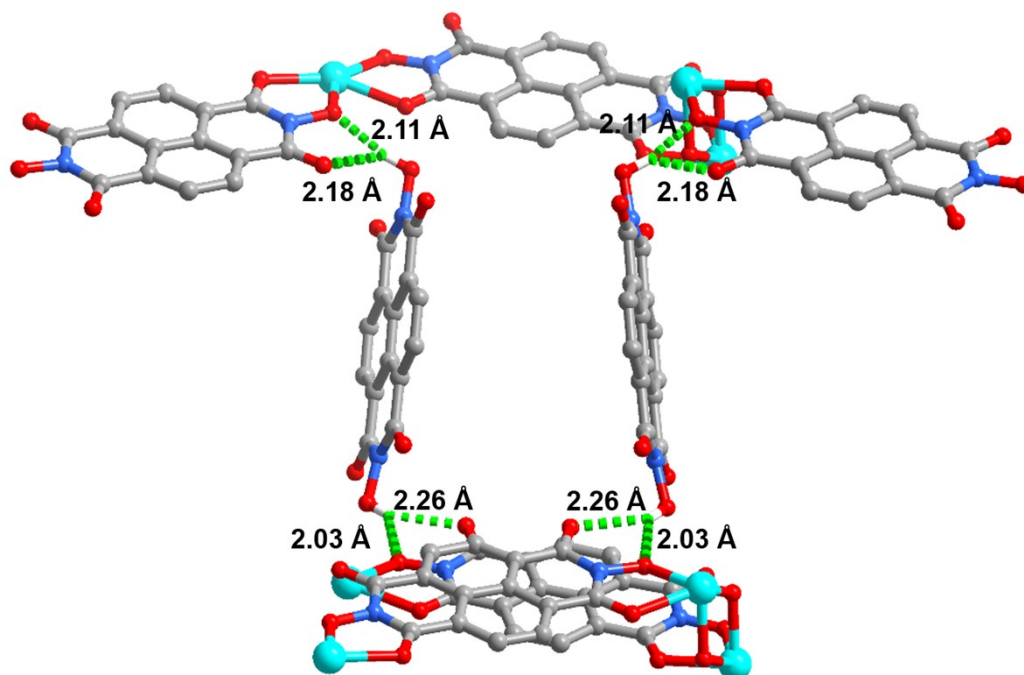


Figure S5. The uncoordinated H_2NDI ligands were located in the porous channel, and their O-H groups formed strong hydrogen bonds with the carbonyl oxygen from the coordinated NDI^{2-} ligands in the framework (O-H \cdots O distances in the ranges of 2.03-2.26 Å).

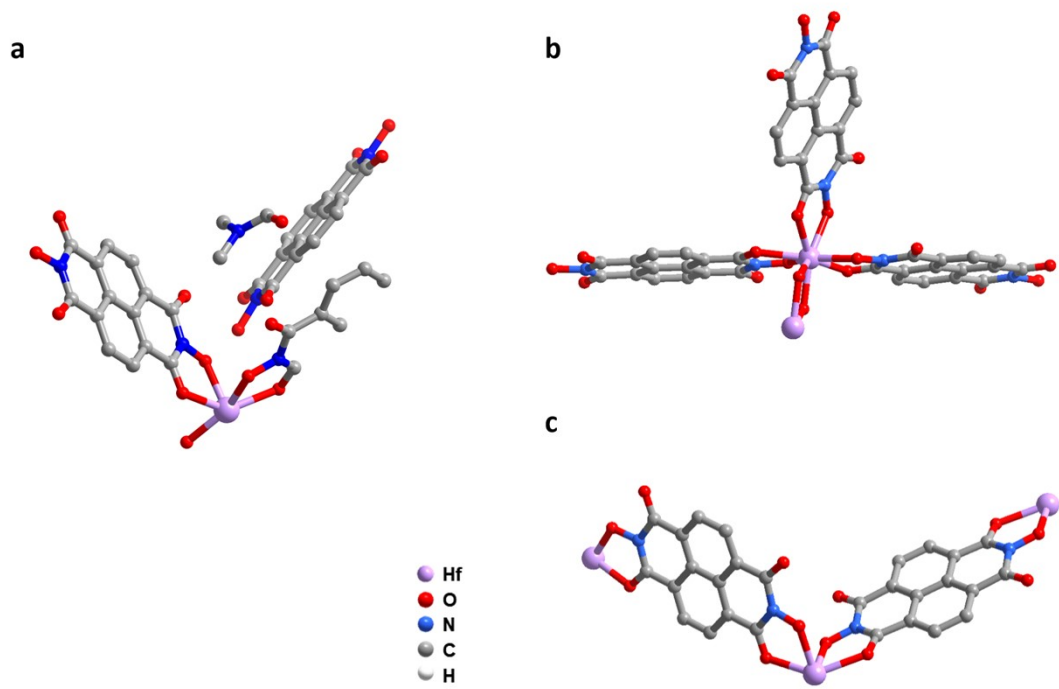


Figure S6. (a) The asymmetric unit of **Hf-NDI**. (b) The coordination environment of the metal ion. (c) The coordination mode of the NDI ligand. All hydrogen atoms were omitted for clarity.

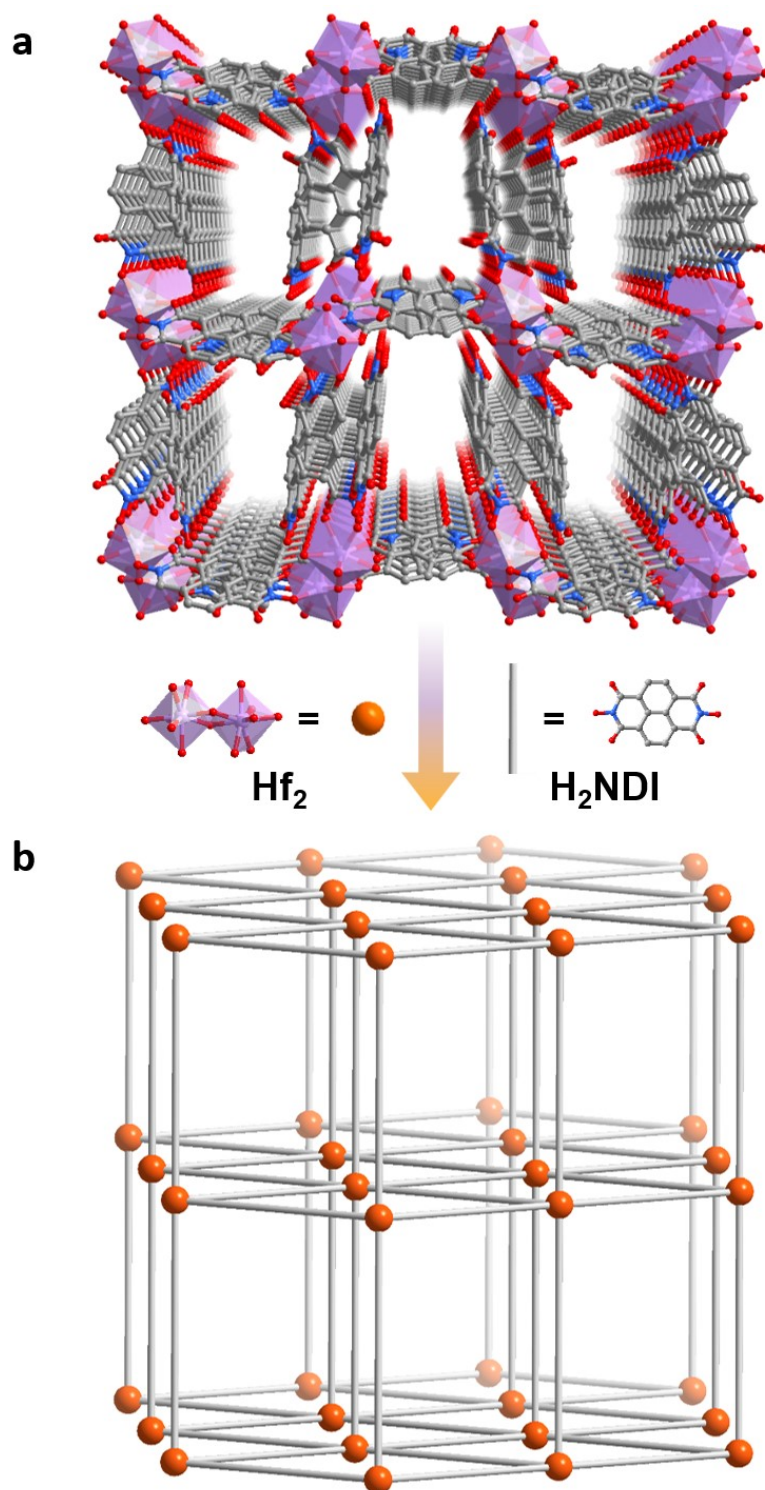


Figure S7. (a) The three-dimensional structural of **Hf-NDI**. All hydrogen atoms are omitted for clarity. Hf, pink, O, red, C, gray, N, blue. (b) Regarding the binuclear Hf_2 unit as a 6-connected code, and the NDI^{2-} ligand as a 2-connected linker, **Hf-NDI** can be simplified to *pcu* topology.

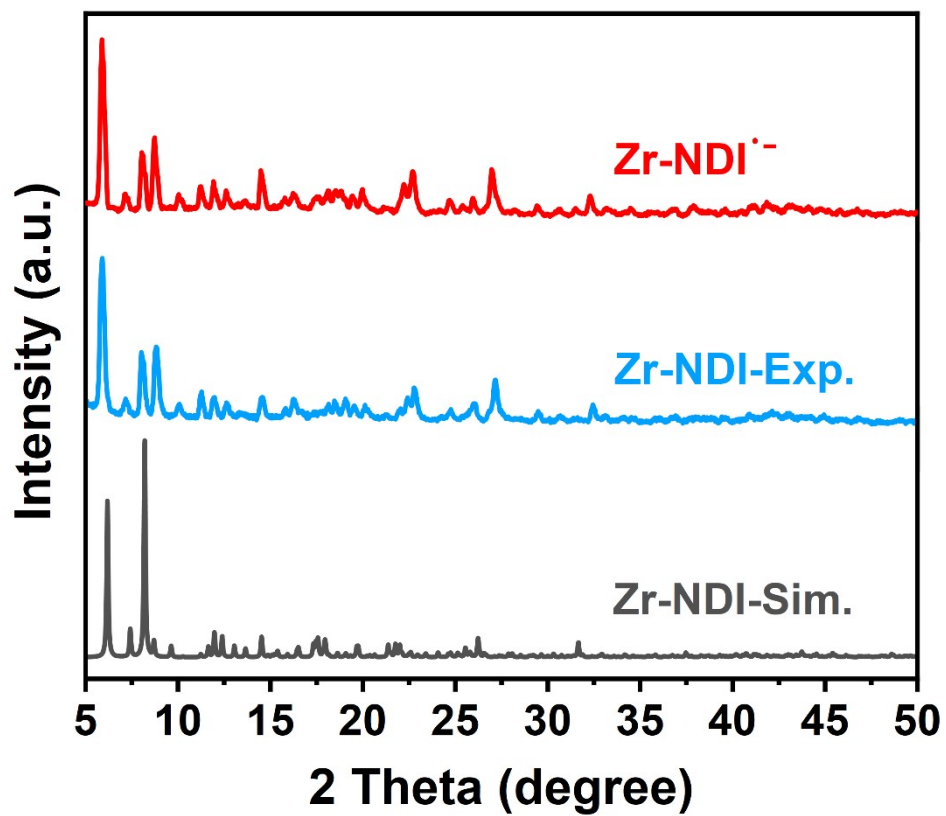


Figure S8. The PXRD patterns of the simulated, experimental Zr-NDI samples and TEA-activated Zr-NDI⁻.

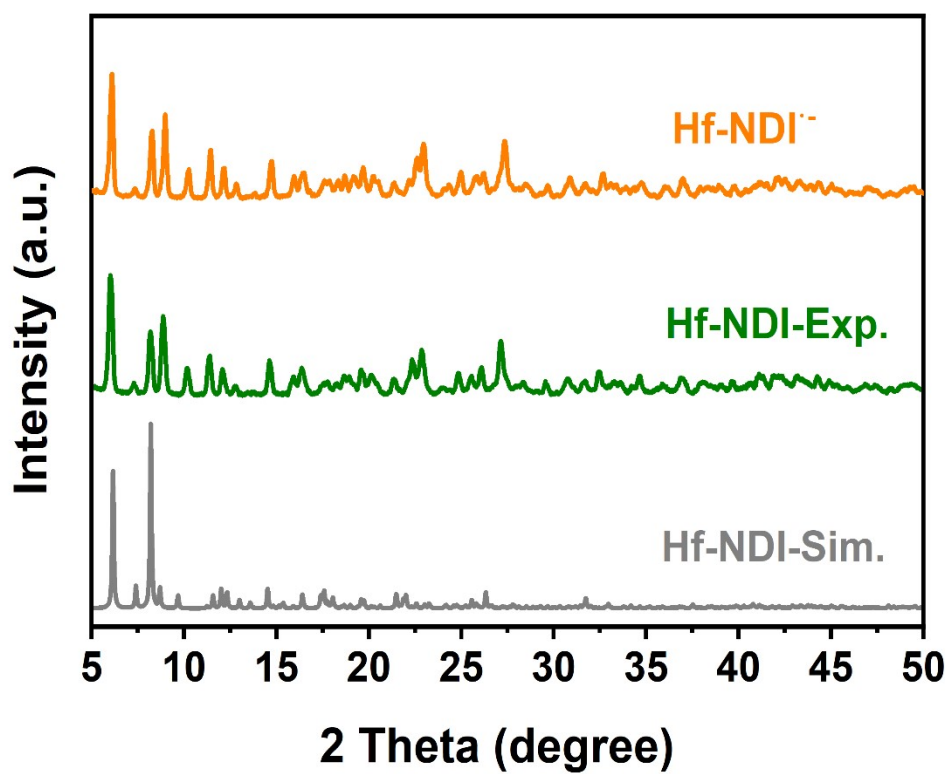


Figure S9. The PXRD patterns of the simulated, experimental **Hf-NDI** samples and TEA-activated **Hf-NDI⁻**.

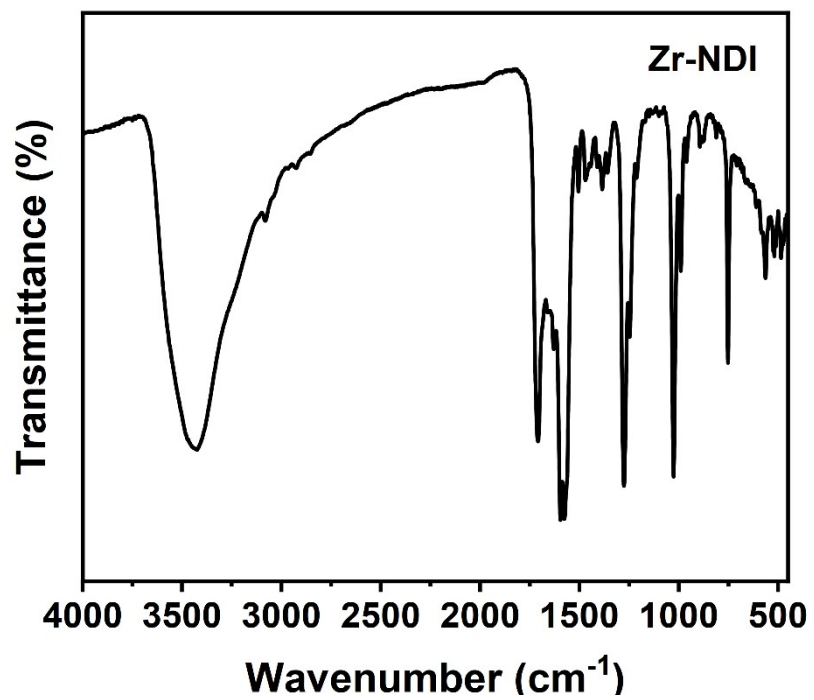


Figure S10. The Fourier transform infrared spectroscopy (FT-IR) spectra of **Zr-NDI**.

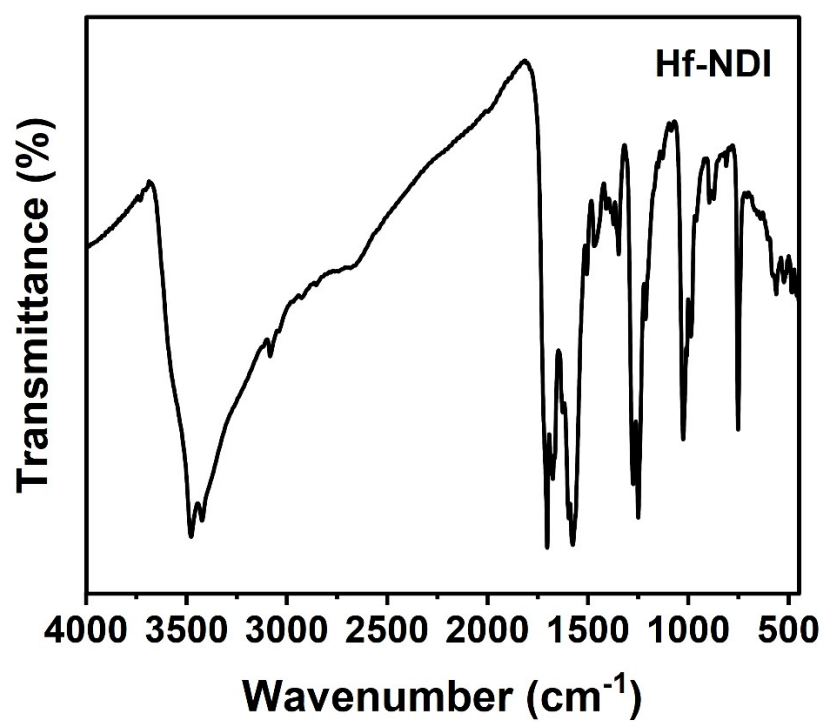


Figure S11. The Fourier transform infrared spectroscopy (FT-IR) spectra of **Hf-NDI**.

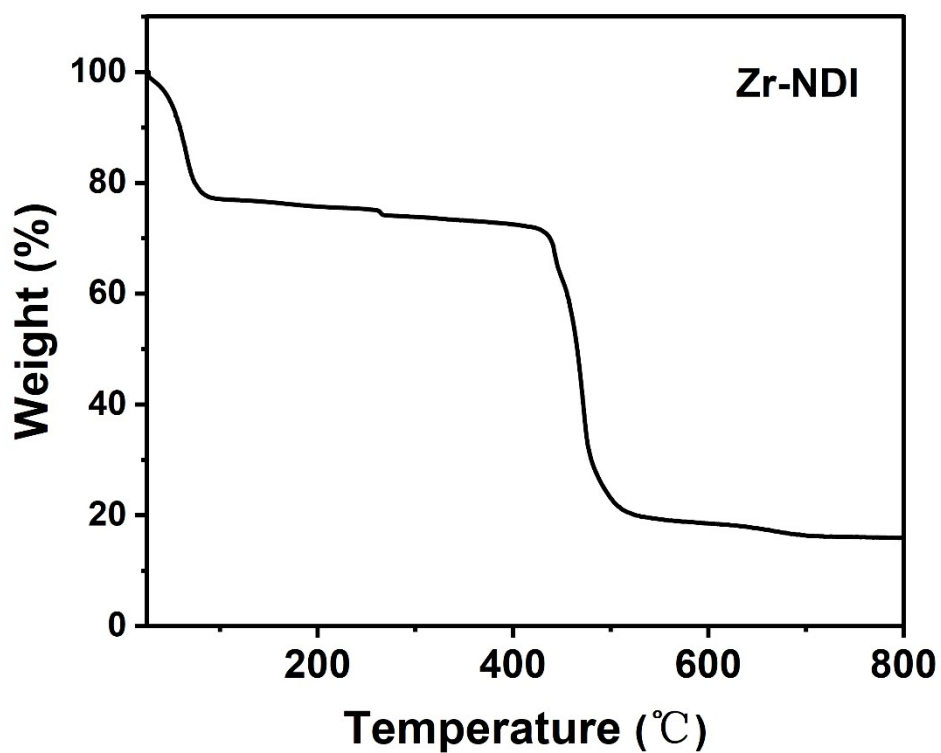


Figure S12. Thermogravimetric curve of **Zr-NDI** measured in air atmosphere from room temperature to 800 °C with the heating rate of 10 °C min⁻¹.

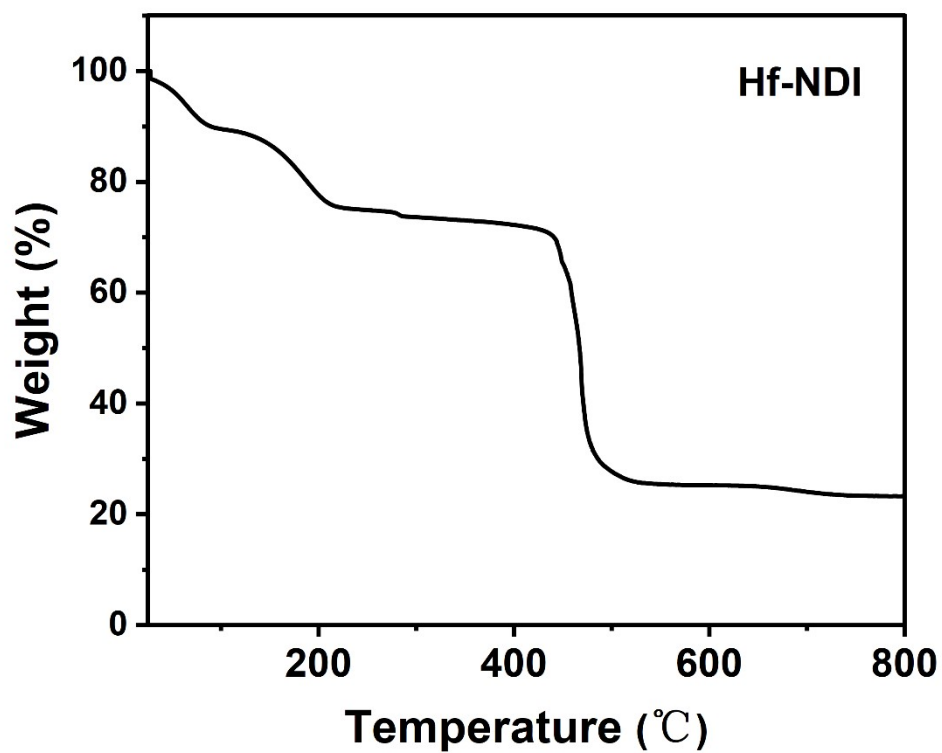


Figure S13. The Thermogravimetric curve of **Hf-NDI** measured in air atmosphere from room temperature to 800 °C with the heating rate of 10 °C min⁻¹.

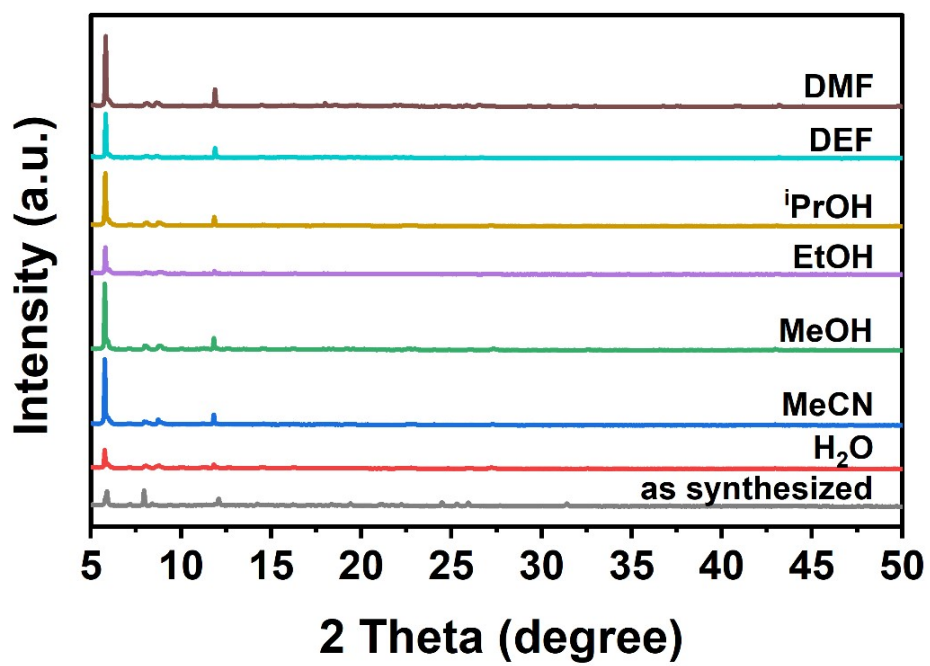


Figure S14. The PXRD patterns of Zr-NDI samples after immersed in different solvents for 24 h.

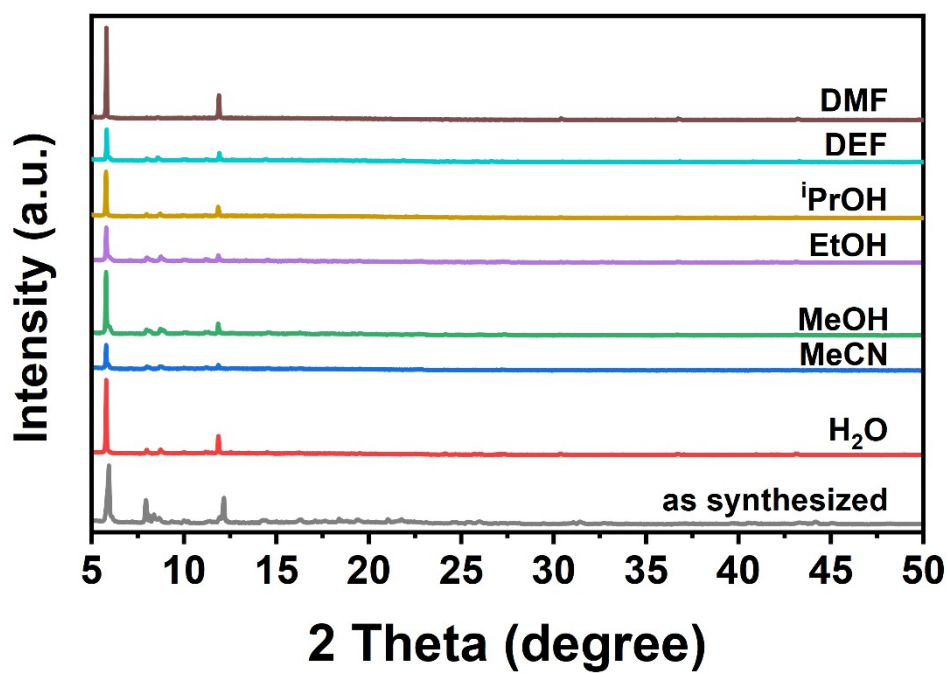


Figure S15. The PXRD patterns of Hf-NDI samples after immersed in different solvents for 24 h.

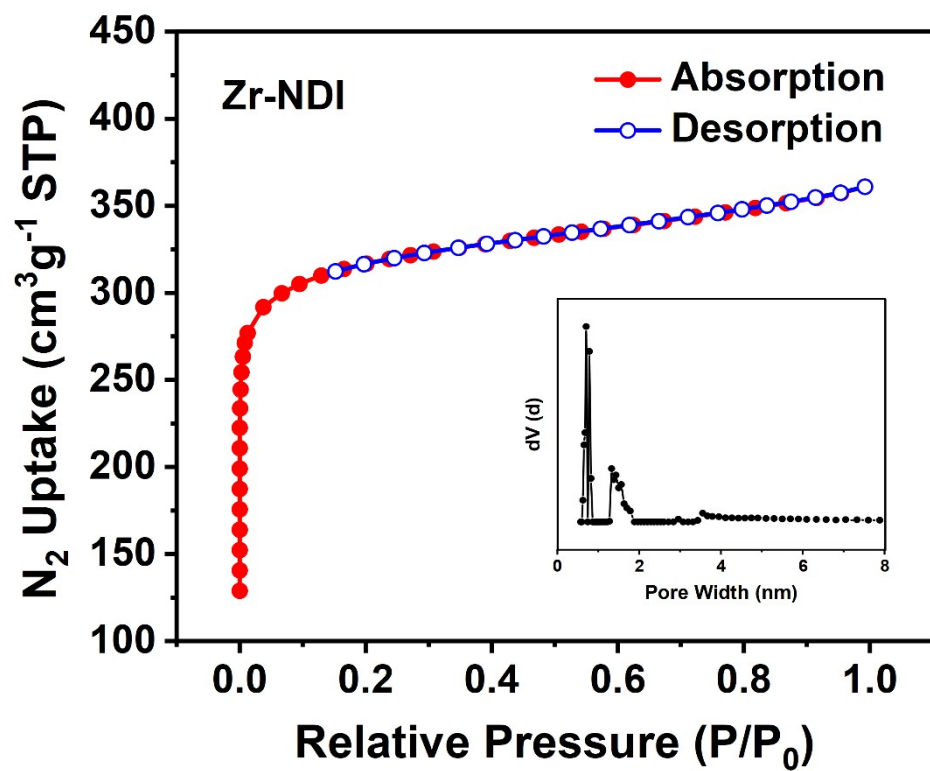


Figure S16. The N₂ adsorption isotherm (77 K) and pore size distribution of Zr-NDI.

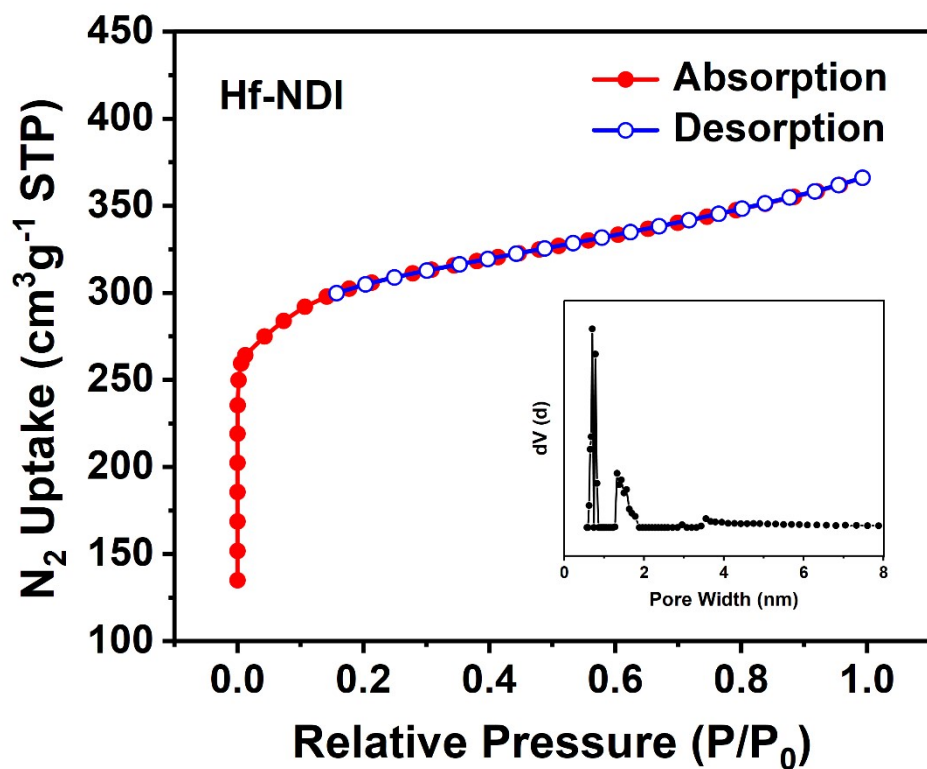


Figure S17. The N_2 adsorption isotherm (77 K) and pore size distribution of **Hf-NDI**.

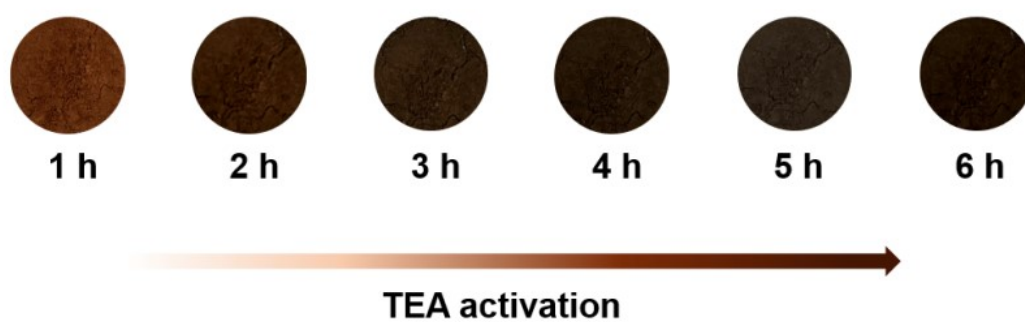


Figure S18. The pictures of the crystal sample of **Zr-NDI** under the TEA atmosphere for different time. Obviously, the color of the crystal powder changed gradually from red to black.

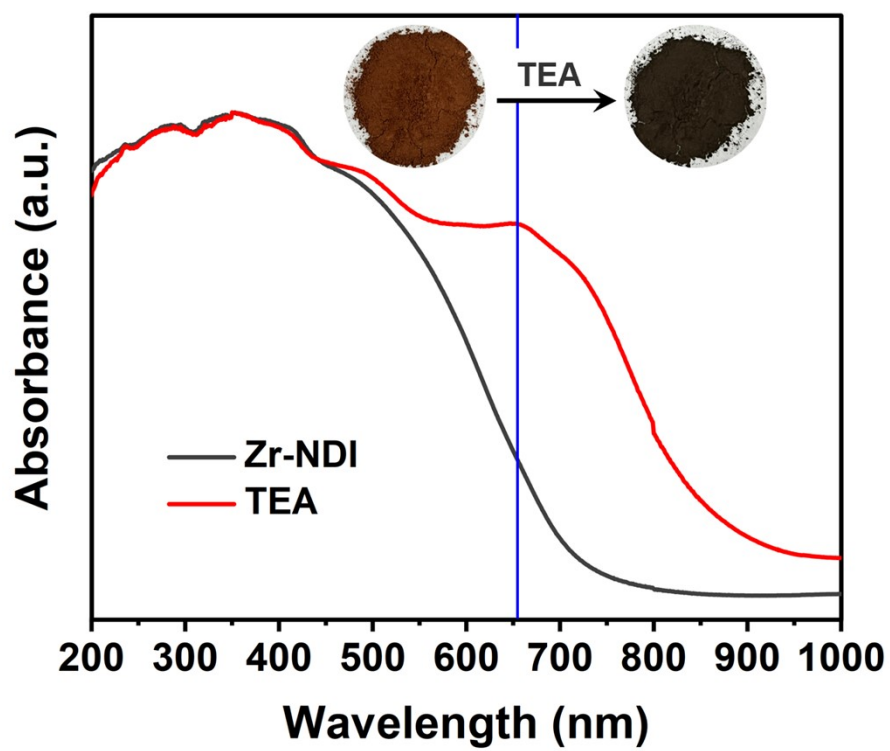


Figure S19. The UV-Vis diffuse reflection spectra of Zr-NDI before and after activated by TEA.

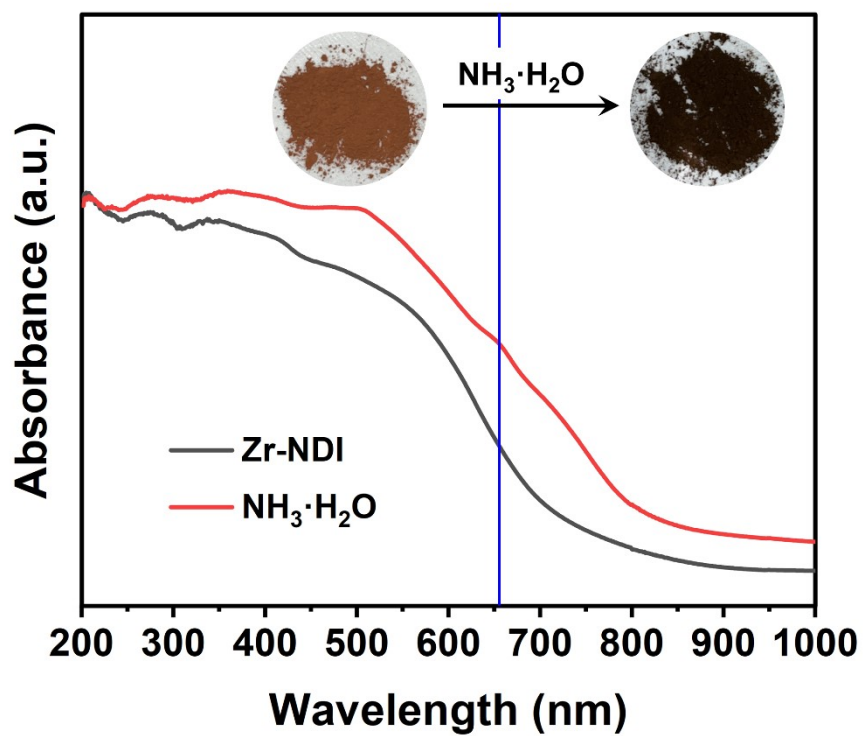


Figure S20. The UV-Vis diffuse reflection spectra of **Zr-NDI** before and after activated by ammonia.

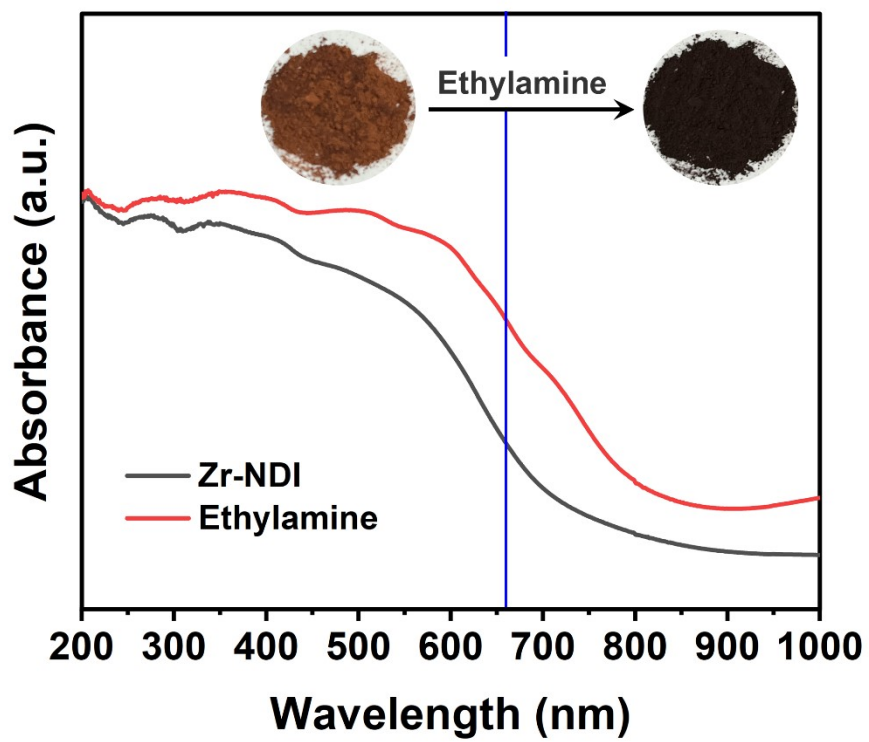


Figure S21. The UV-Vis diffuse reflection spectra of **Zr-NDI** before and after activated by ethylamine.

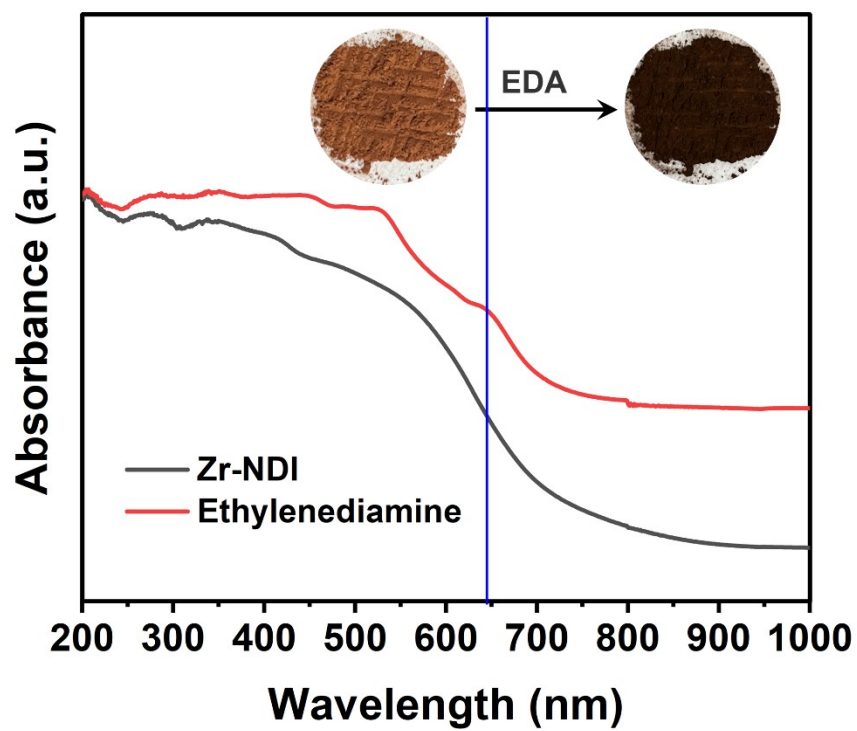


Figure S22. The UV-Vis diffuse reflection spectra of **Zr-NDI** before and after activated by ethylenediamine.

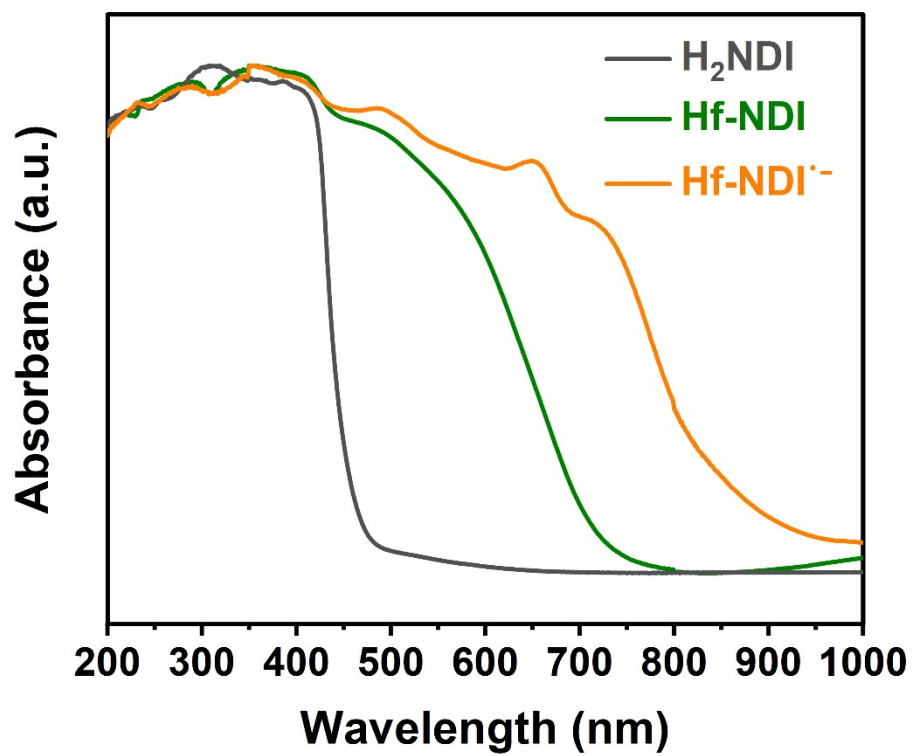


Figure S23. UV/Vis absorption spectra of ligand (gray), Hf-NDI (green) and radical Hf-NDI^{•-} (orange).

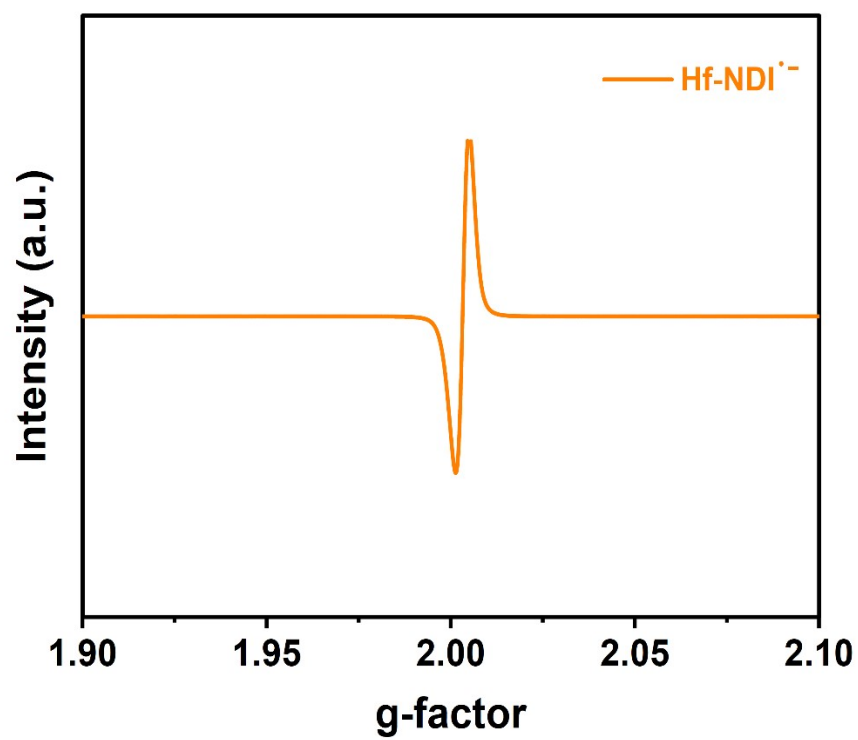


Figure S24. EPR spectra of radical Hf-NDI^{•-}.

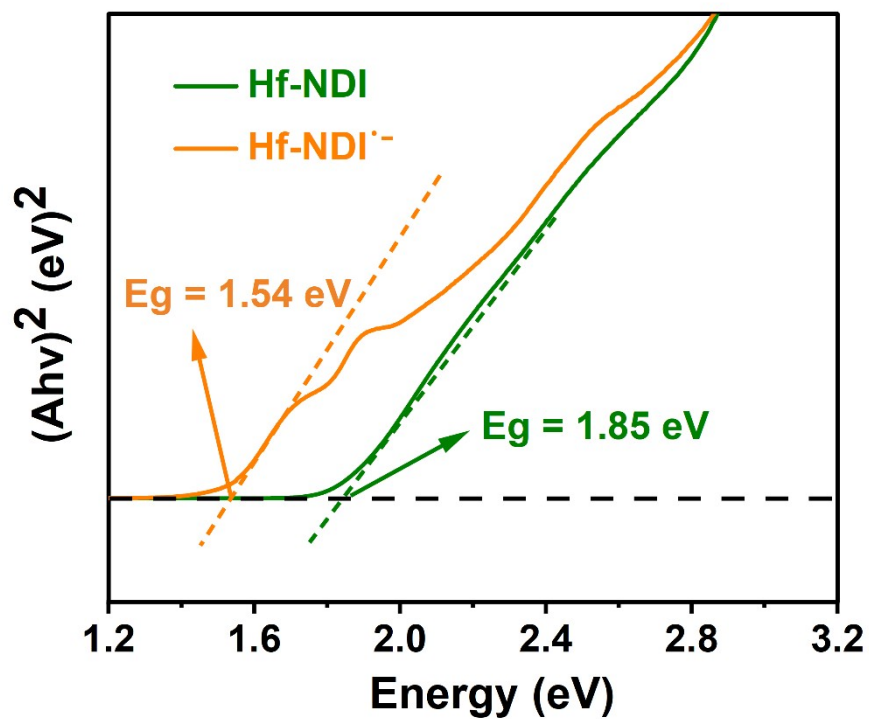


Figure S25. Tauc plots of Hf-NDI (green) and Hf-NDI⁻ (orange) determined by the Kubelka–Munk formula from the original UV/Vis-NIR DRS spectra.

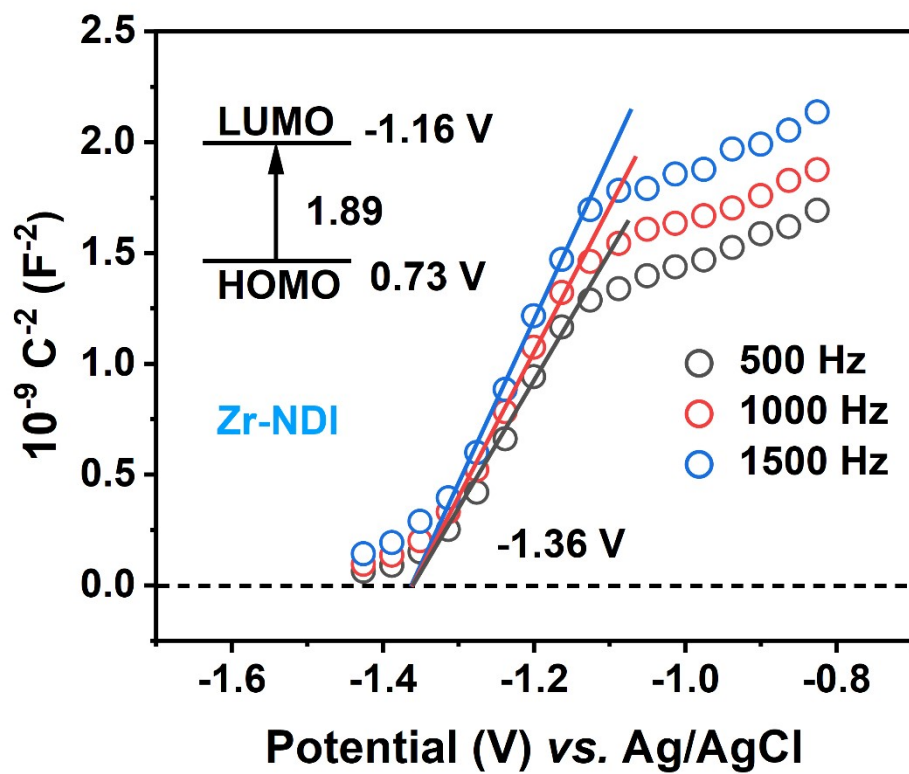


Figure S26. Mott-Schottky plot measurement for Zr-NDI. Inset: Energy diagram of the HOMO and LUMO levels of Zr-NDI.

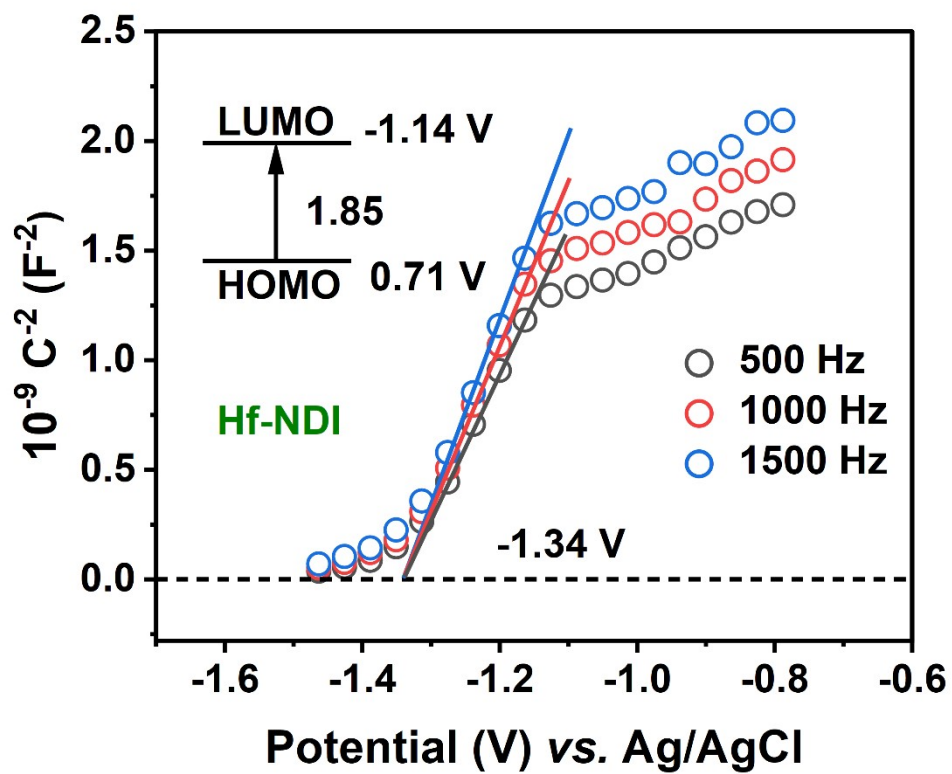


Figure S27. Mott-Schottky plot measurement for Hf-NDI. Inset: Energy diagram of the HOMO and LUMO levels of Hf-NDI.

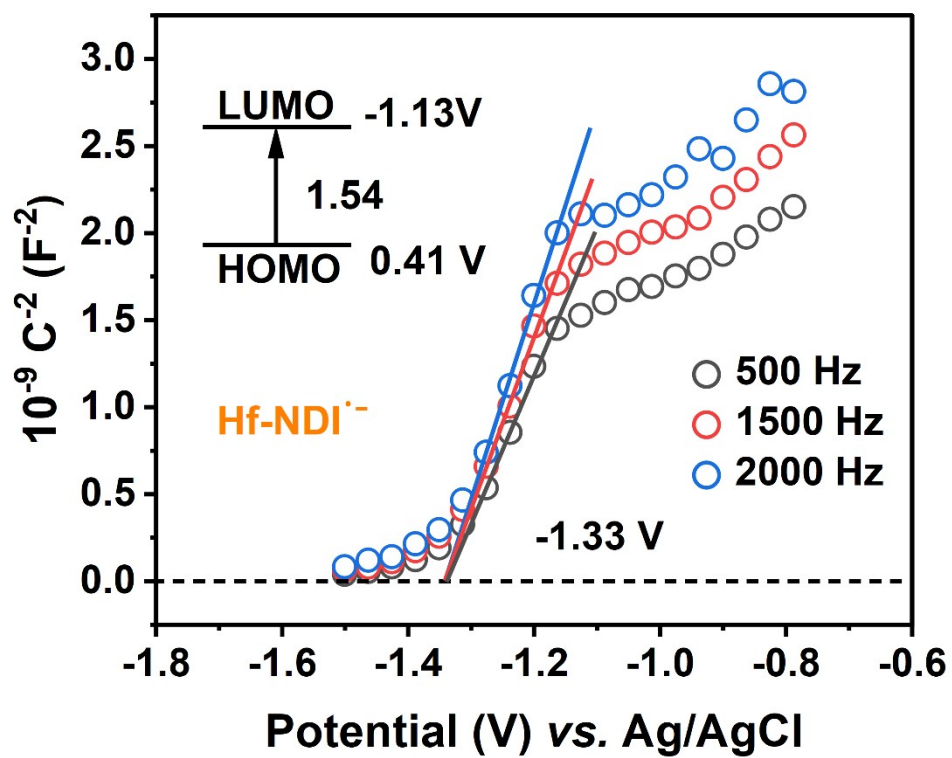


Figure S28. Mott-Schottky plot measurement for $\text{Hf-NDI}^{\bullet-}$. Inset: Energy diagram of the HOMO and LUMO levels of $\text{Hf-NDI}^{\bullet-}$.

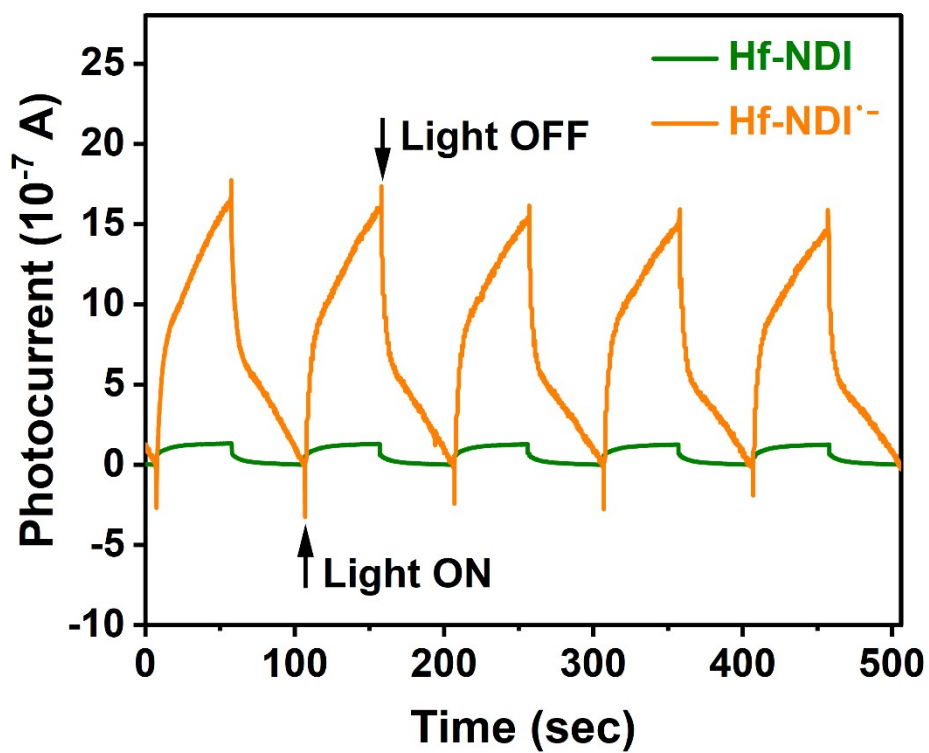


Figure S29. Transient photocurrent response of Hf-NDI (green) and Hf-NDI^{•-} (orange) under Xe lamp irradiation.

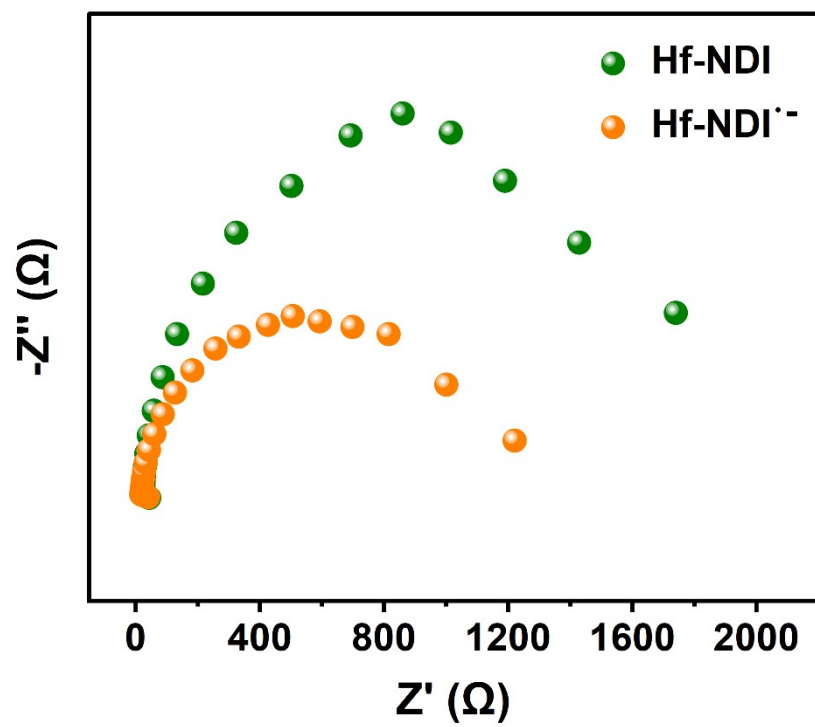


Figure S30. Electrochemical impedance spectroscopy (EIS) Nyquist plots of **Hf-NDI** (green) and **Hf-NDI⁻** (orange).

Table S2. Screening of solvent amount and atmosphere for photocatalytic reaction.

| Entry | Catalyst | Solvent amount | Atmosphere | Time | Con. [%] | Sel. of 2MBZ [%] |
|-------|----------------------|--|----------------|------|----------|------------------|
| 1 | Zr-NDI ²⁺ | C ₂ H ₅ OH 2 mL | Ar | 12 h | 7.2 | 100 |
| 2 | Zr-NDI ²⁺ | C ₂ H ₅ OH 5 mL | Ar | 12 h | 68.8 | 100 |
| 3 | Zr-NDI ²⁺ | C ₂ H ₅ OH 10 mL | Ar | 12 h | > 99 | 100 |
| 4 | Zr-NDI ²⁺ | C ₂ H ₅ OH 10 mL | Air | 12 h | 96.7 | 100 |
| 5 | Zr-NDI ²⁺ | C ₂ H ₅ OH 10 mL | O ₂ | 12 h | 73.8 | 100 |

The results of atmosphere screening experiments showed that the best catalytic performance was achieved under Ar, with the yield as high as 99%. When it changed to air or O₂, the yield dropped to 96.7% and 73.8%, respectively, which not only showed a decreasing trend, but decreased more dramatically as the oxygen content increased. This is because this reaction undergoes radical-induced cross-coupling route, in which •CH(CH₃)OH is the carbon radical reactive species. Because O₂ may restrain the generation of •CH(CH₃)OH radical, thus, under O₂, the yield dropped significantly.

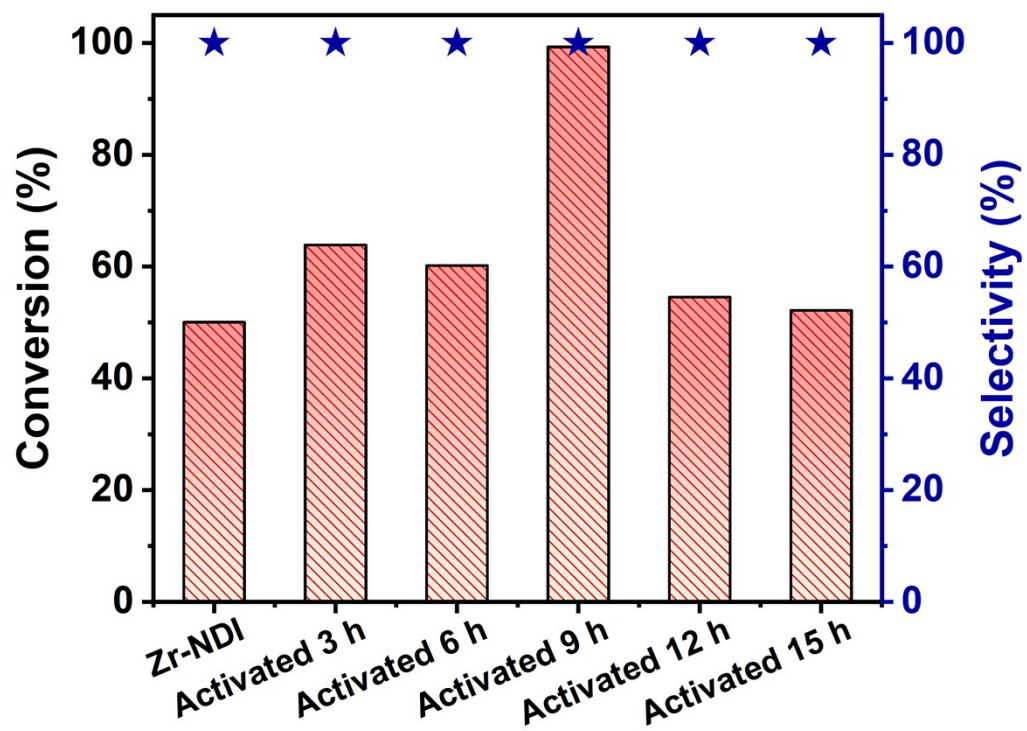


Figure S31. Photocatalytic performance of original Zr-NDI and Zr-NDI⁻ with different TEA activation time under the optimal reaction conditions.

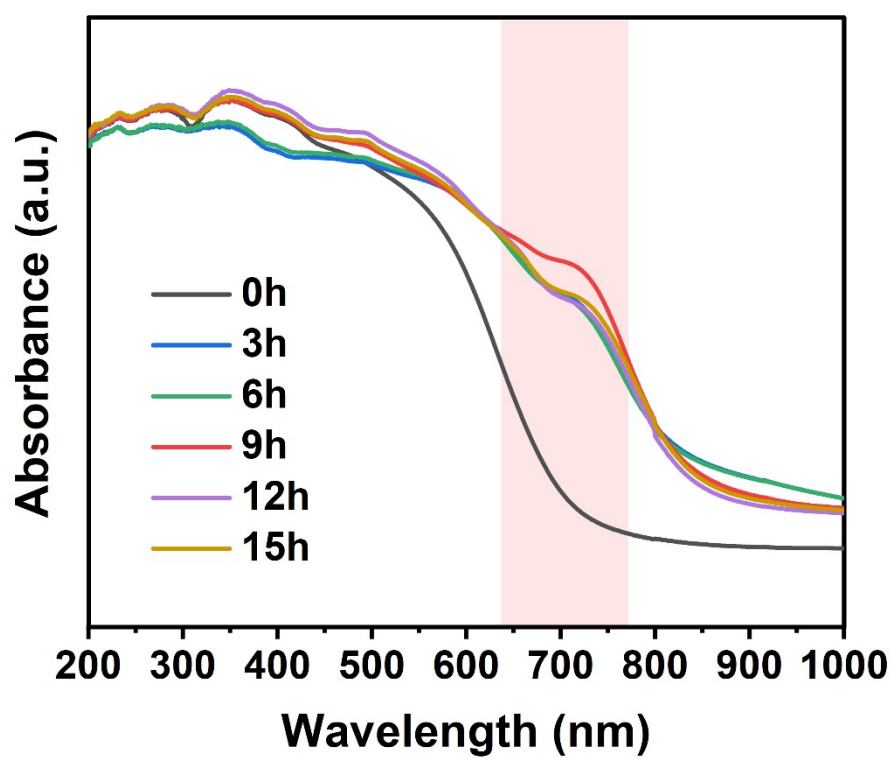


Figure S32. UV/Vis diffuse reflection spectrum of Zr-NDI⁻ under different TEA activation time.

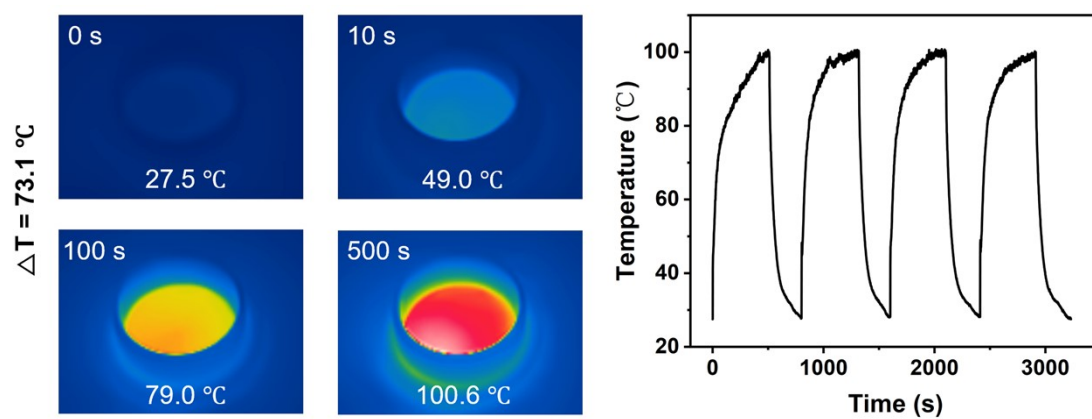


Figure S33. Photothermal images of Zr-NDI⁻ and cycling tests of temperature changes of Zr-NDI⁻ under irradiation.

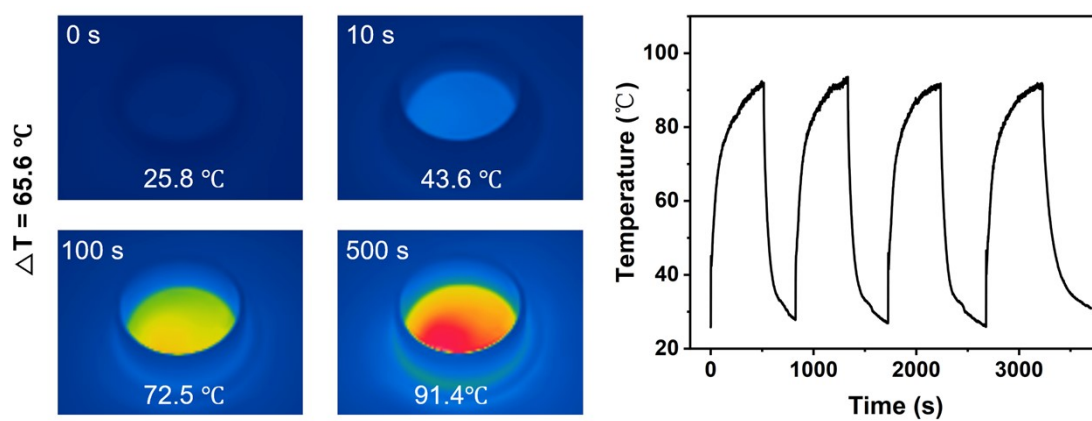


Figure S34. Photothermal images of **Zr-NDI** and cycling tests of temperature changes of **Zr-NDI** under irradiation.

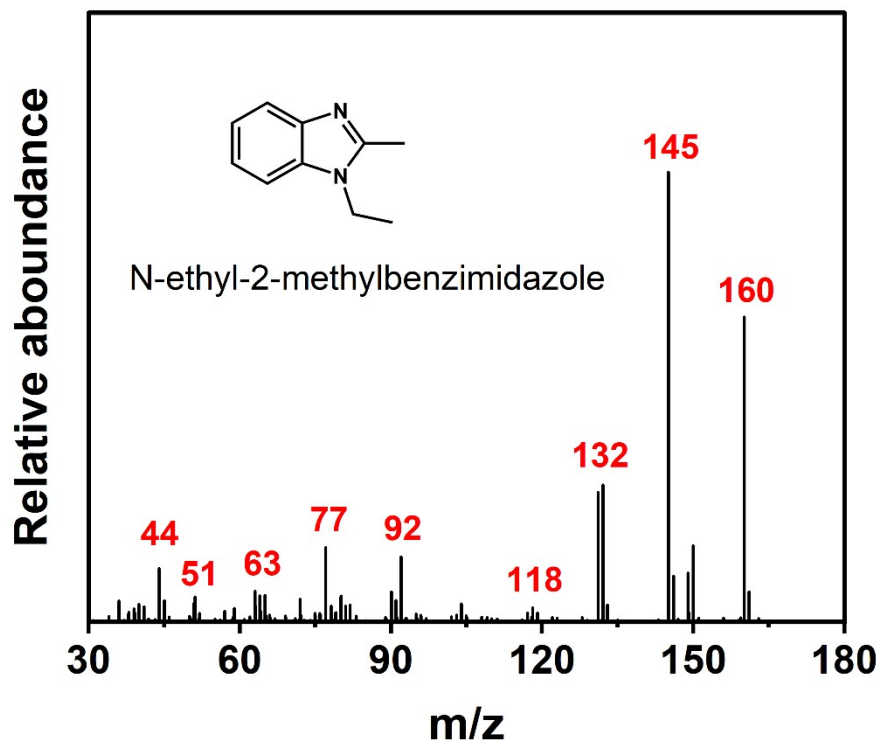


Figure S35. The Mass spectrum of by-product N-ethyl-2-methylbenzimidazole (NE2MBZ).

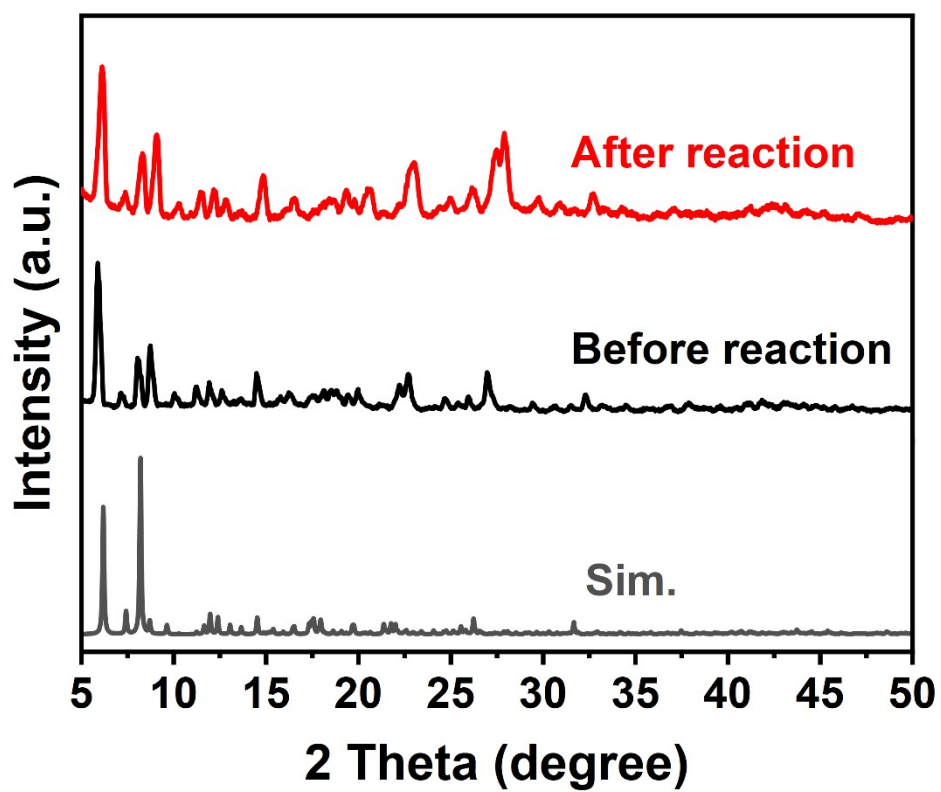


Figure S36. The PXRD patterns of Zr-NDI⁻ before and after reaction.

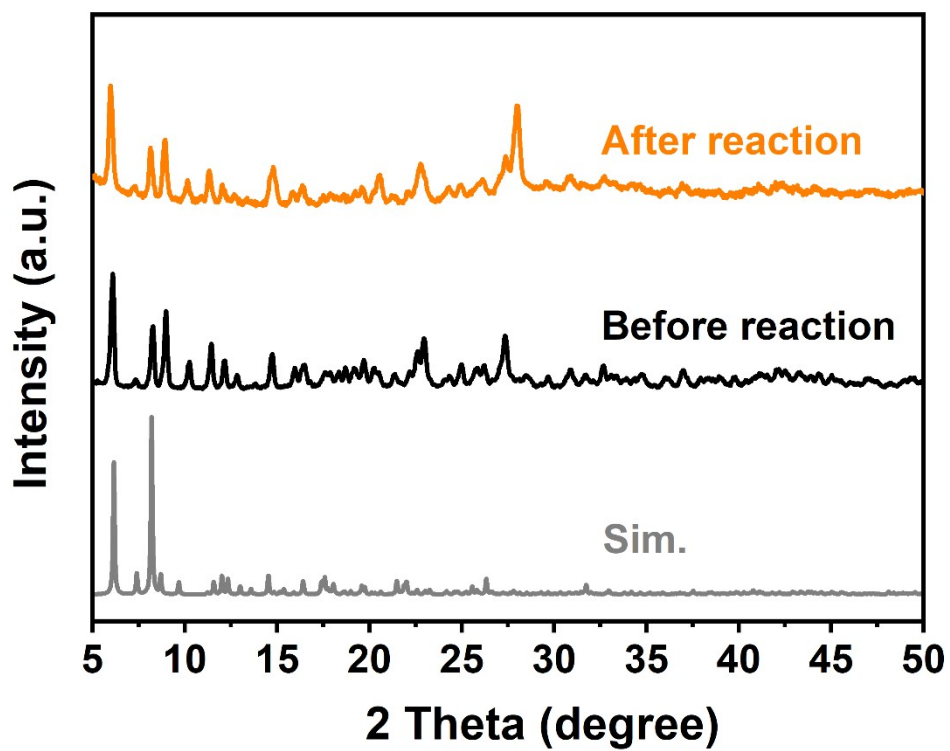


Figure S37. The PXRD patterns of **Hf-NDI⁻** before and after reaction.

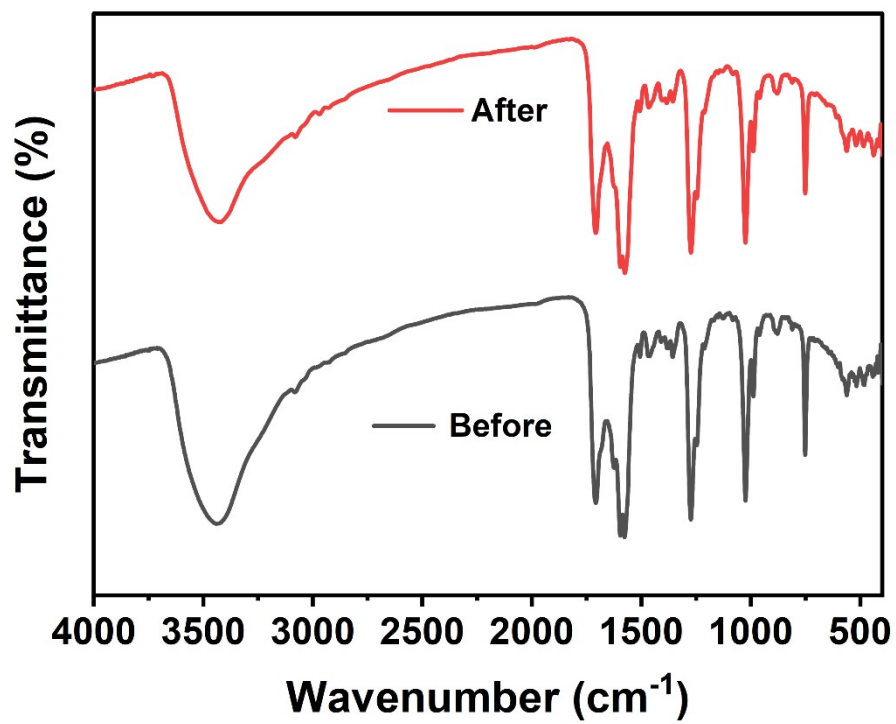


Figure S38. The FT-IR spectrum of Zr-NDI⁻ before and after the catalytic reaction.

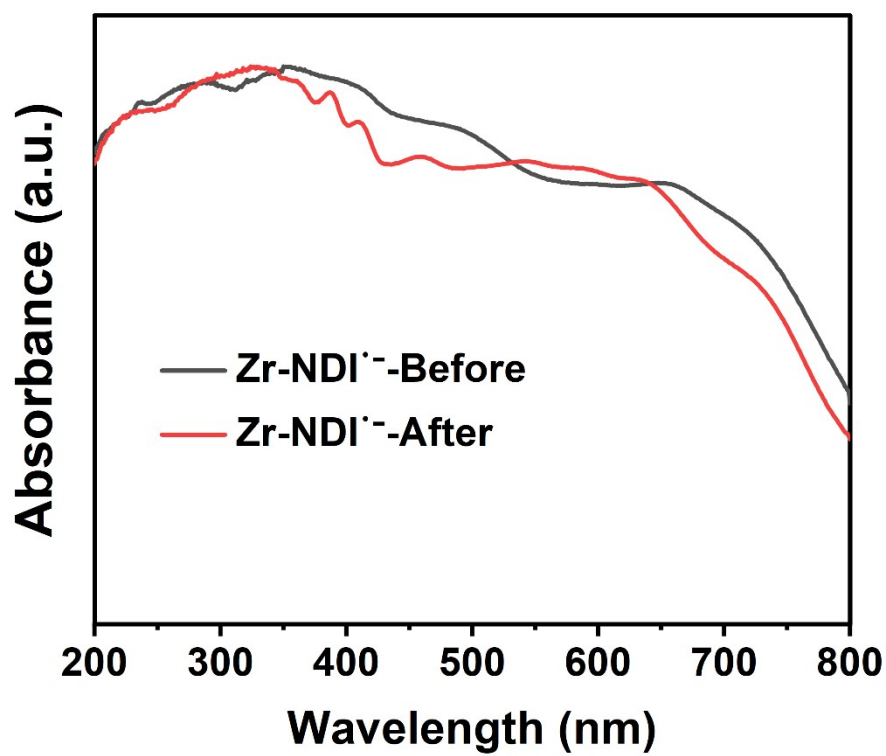


Figure S39. UV/Vis diffuse reflection spectrum of Zr-NDI⁻ after reaction.

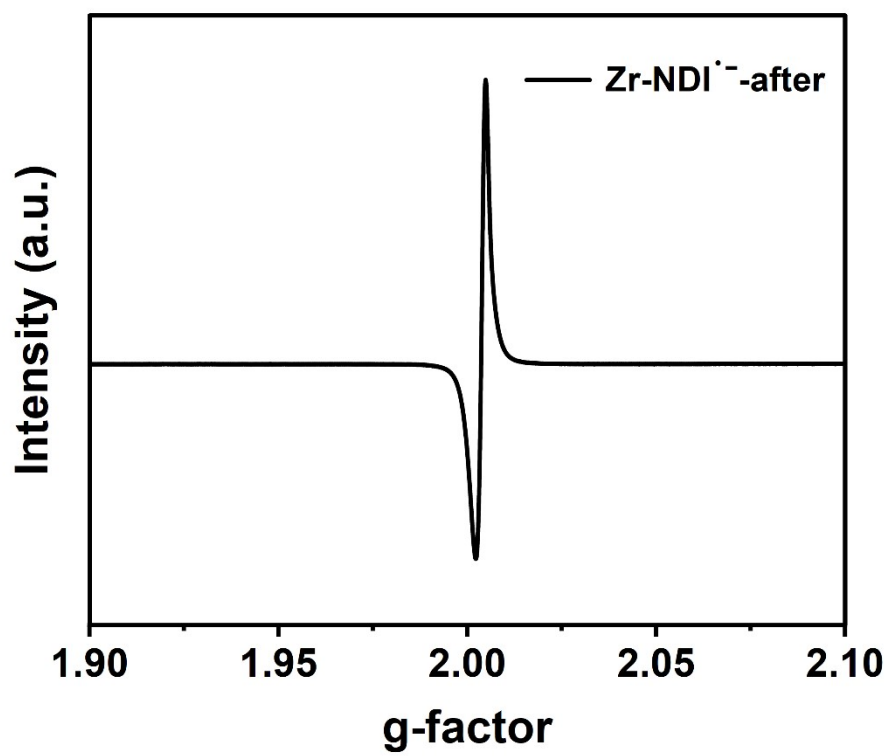
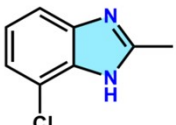
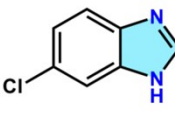
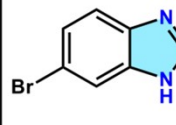


Figure S40. EPR spectra of Zr-NDI^{•-} after reaction.

Table S3. Photocatalytic benzimidazoles synthesis system over different catalysts.

| Catalyst | OPD [mmol] | Atmosphere | Light source | Time | Con. [%] | Sel. of 2MBZ [%] | Ref. |
|--------------------------------------|------------|----------------|------------------------------------|------|----------|------------------|------------------|
| Zr-NDI ⁻ | 0.05 | Ar | Xe lamp (300nm < λ < 1100nm) | 12 h | > 99 | 100 | This work |
| Au/MIL-101(Fe) | 0.1 | O ₂ | 5W LED lamp (400nm < λ < 780nm) | 12 h | 46.9 | 45.8 | [S8] |
| Pt@MIL-101(Fe) | 0.05 | N ₂ | Xe lamp (400nm < λ < 780nm) | 24 h | 83.4 | 79.8 | [S9] |
| 1Pd/TiO ₂ -V _O | 0.05 | Ar | Xe lamp (320nm < λ < 780nm) | 3 h | > 99 | 92 | [S10] |
| Pt@TiO ₂ | 0.02 | N ₂ | Xe lamp (λ > 300nm) | 2 h | 99 | 93 | [S11] |
| 15Pd/ZnO | 0.05 | Ar | Xe lamp (320nm < λ < 780nm) | 4 h | > 99 | 98 | [S12] |
| C-TiO ₂ | 0.1 | O ₂ | Xe lamp (λ > 420nm) | 4 h | > 99 | 83 | [S13] |

Table S4. Performance comparison of OPD substrates with electron-withdrawing groups over different catalytic systems.

| Entry |  |  |  | Ref. |
|--------------------------------------|---|---|--|------------------|
| Zr-NDI ⁻ | 81 % | 85% | 84% | This work |
| 15Pd/ZnO | — | 9% | — | [S12] |
| 1Pd/TiO ₂ -V _O | — | 57% | 64% | [S10] |
| Au/MIL-101(Fe) | — | 50% | 54% | [S8] |
| Pt@MIL-101(Fe) | — | — | — | [S9] |
| Pt@TiO ₂ | — | 99% | — | [S11] |
| C-TiO ₂ | — | — | — | [S13] |

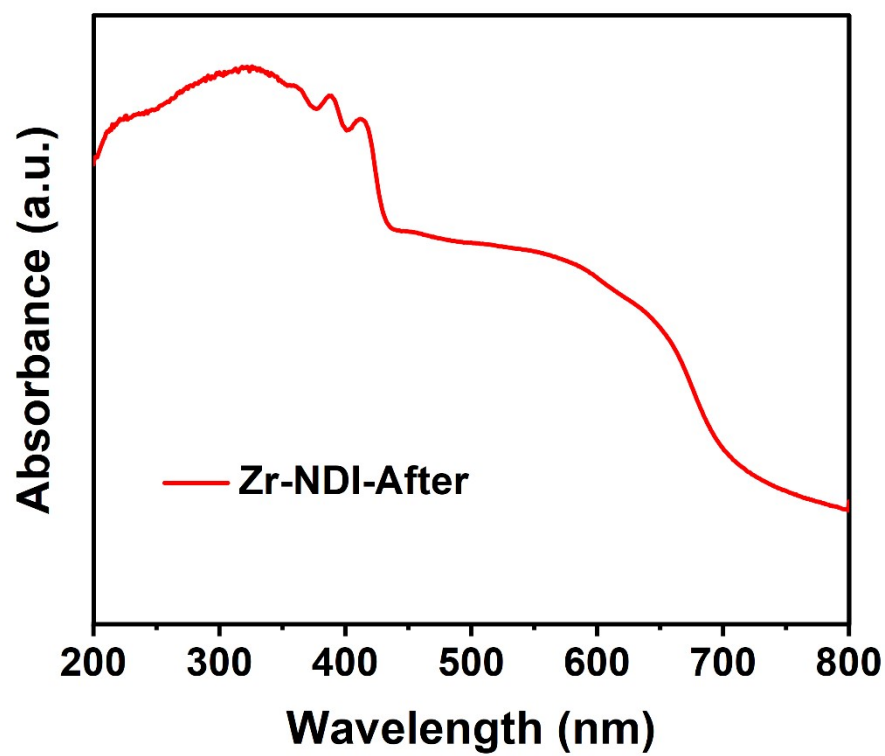


Figure S41. UV/Vis diffuse reflection spectrum of **Zr-NDI** after immersing in ethanol solution of OPD under light.

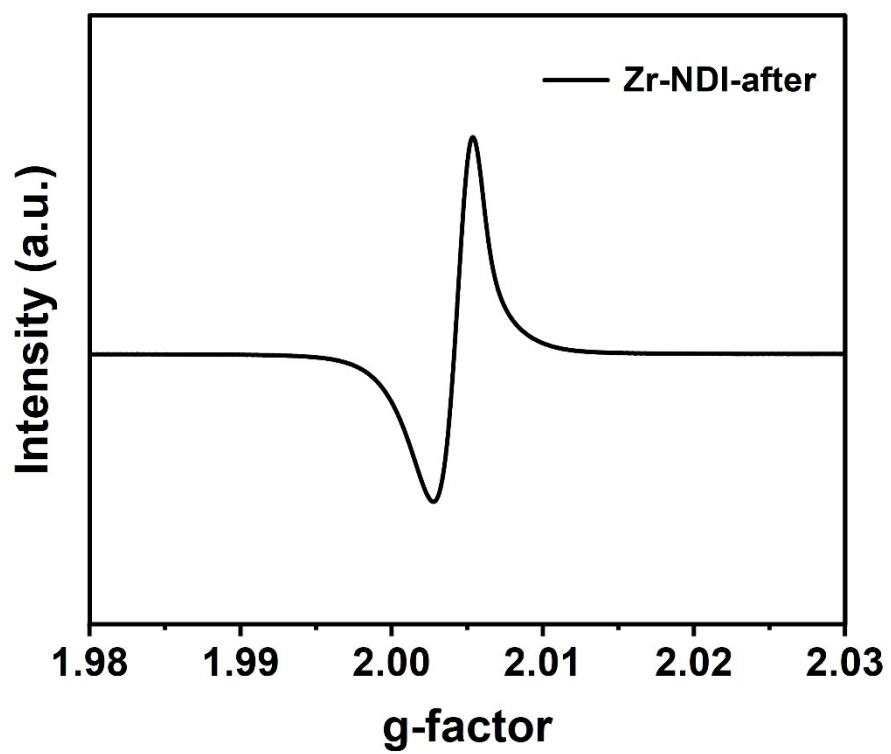


Figure S42. EPR spectra of **Zr-NDI** after immersing in ethanol solution of OPD under light.

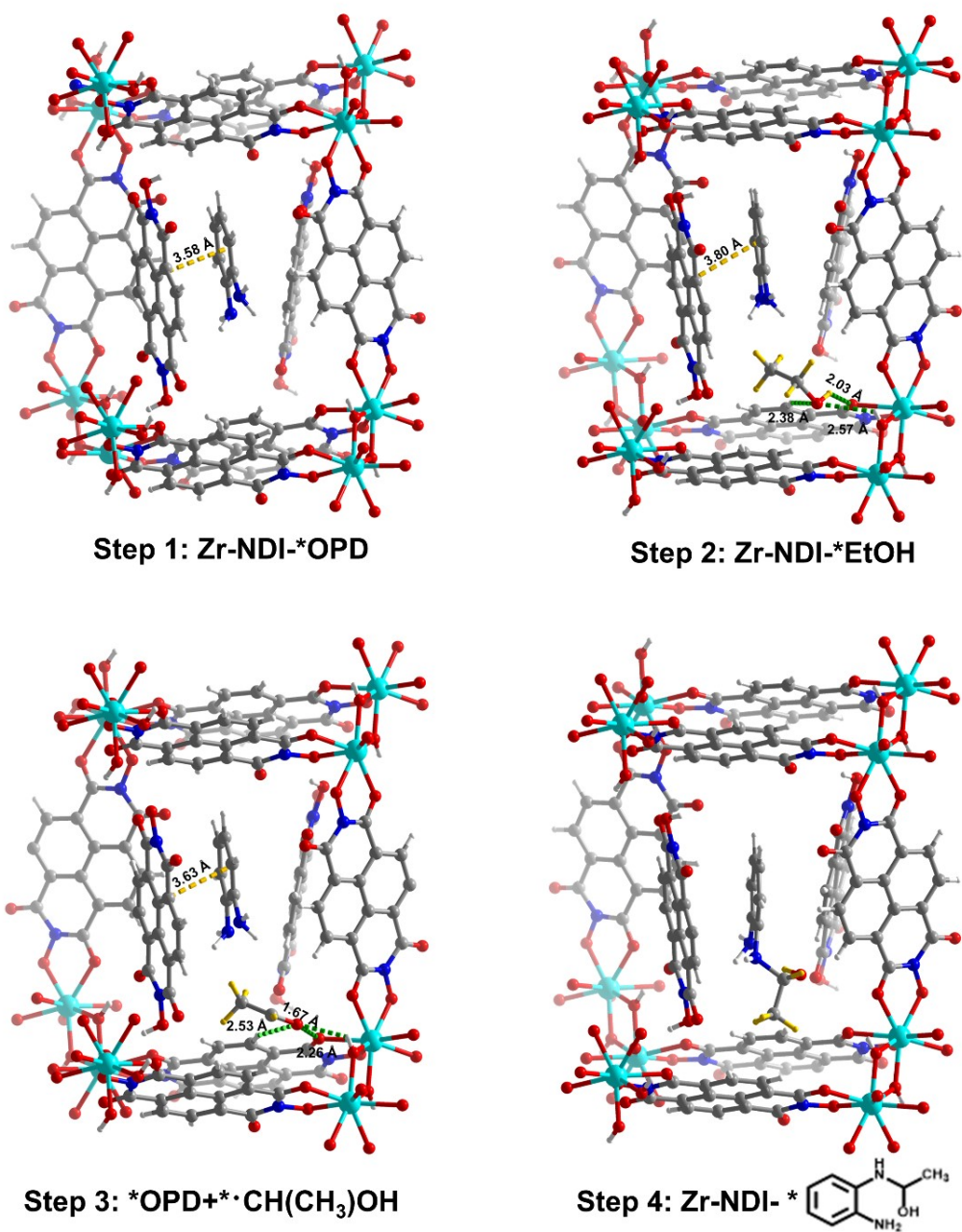


Figure S43. Optimized structures for the reaction intermediates on Zr-NDI.

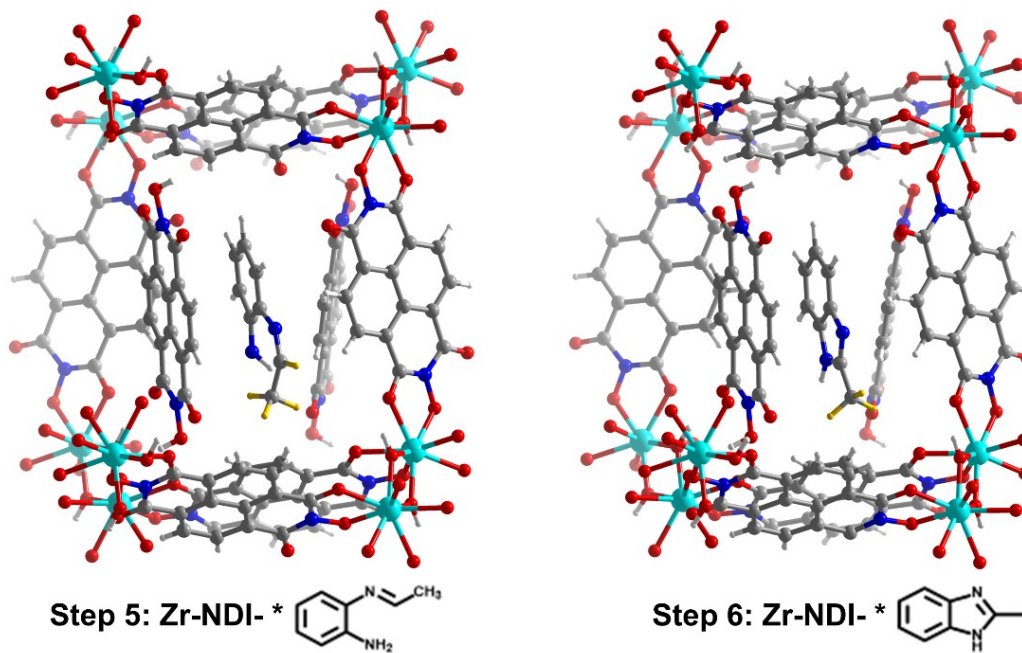


Figure S44. Optimized structures for the reaction intermediates on Zr-NDI.

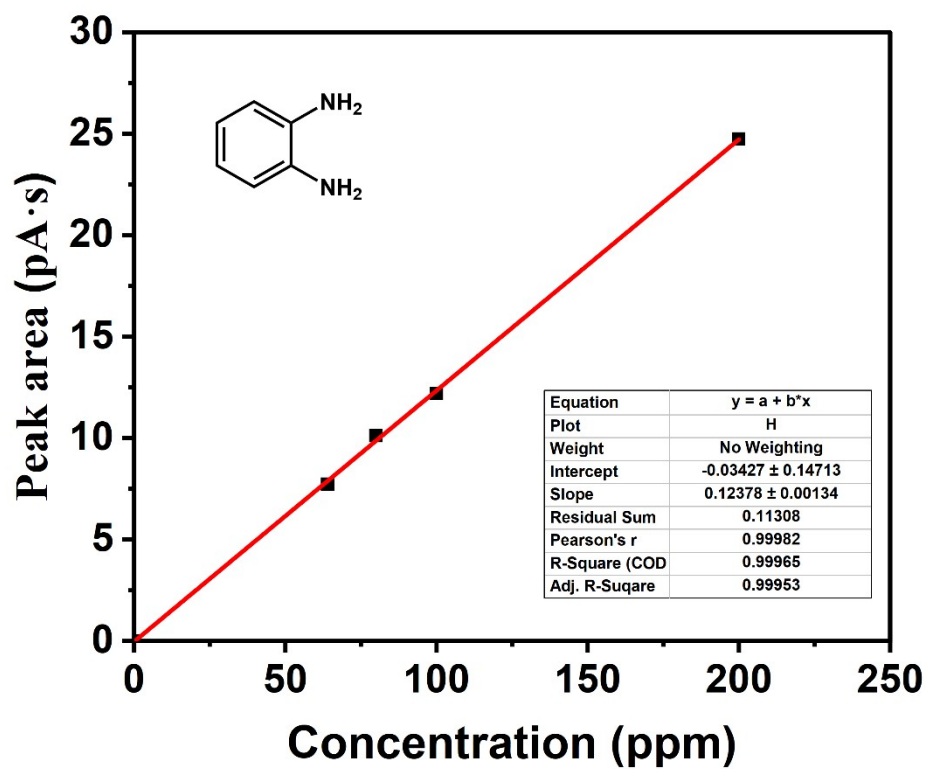


Figure S45. Standard curves of *o*-phenylenediamine by GC analysis.

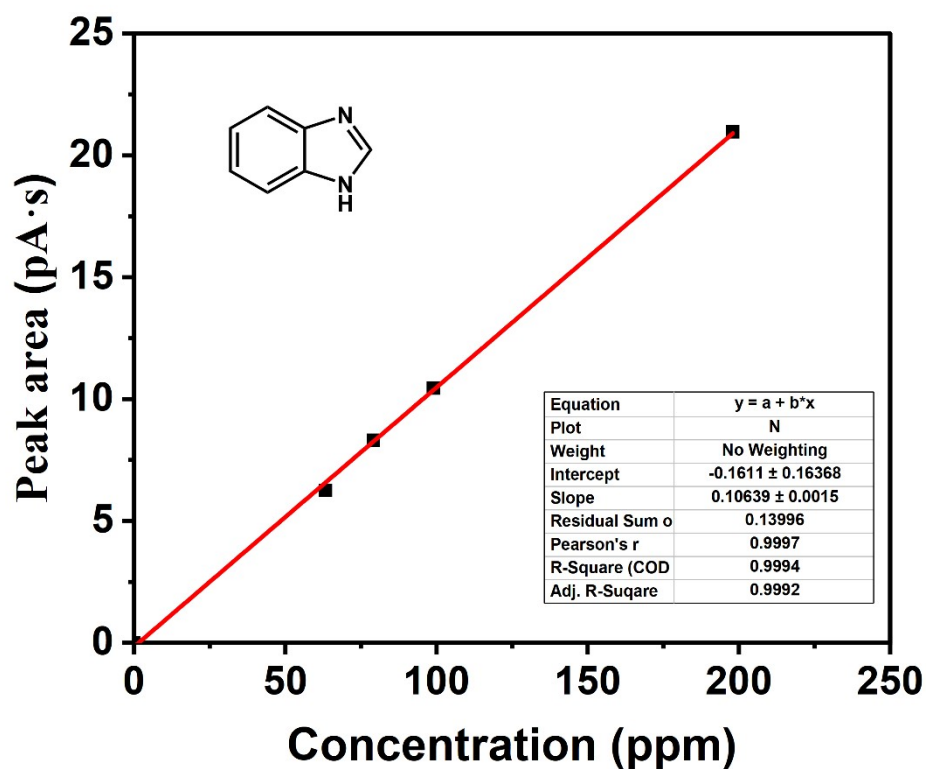


Figure S46. Standard curves of benzimidazole by GC analysis.

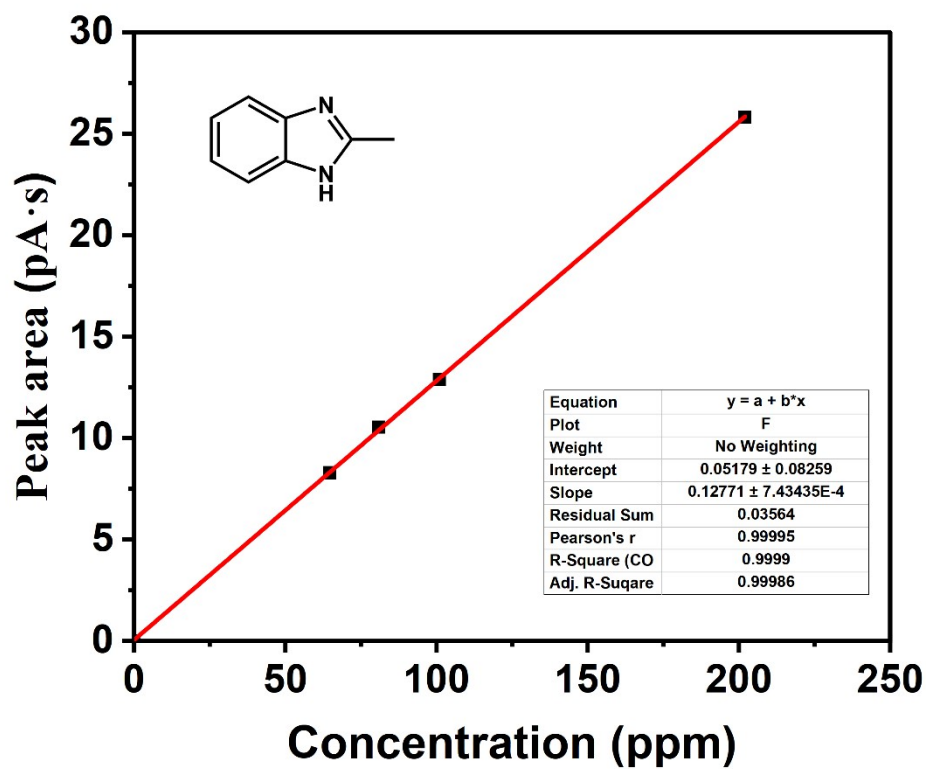


Figure S47. Standard curves of 2-methylbenzimidazole by GC analysis.

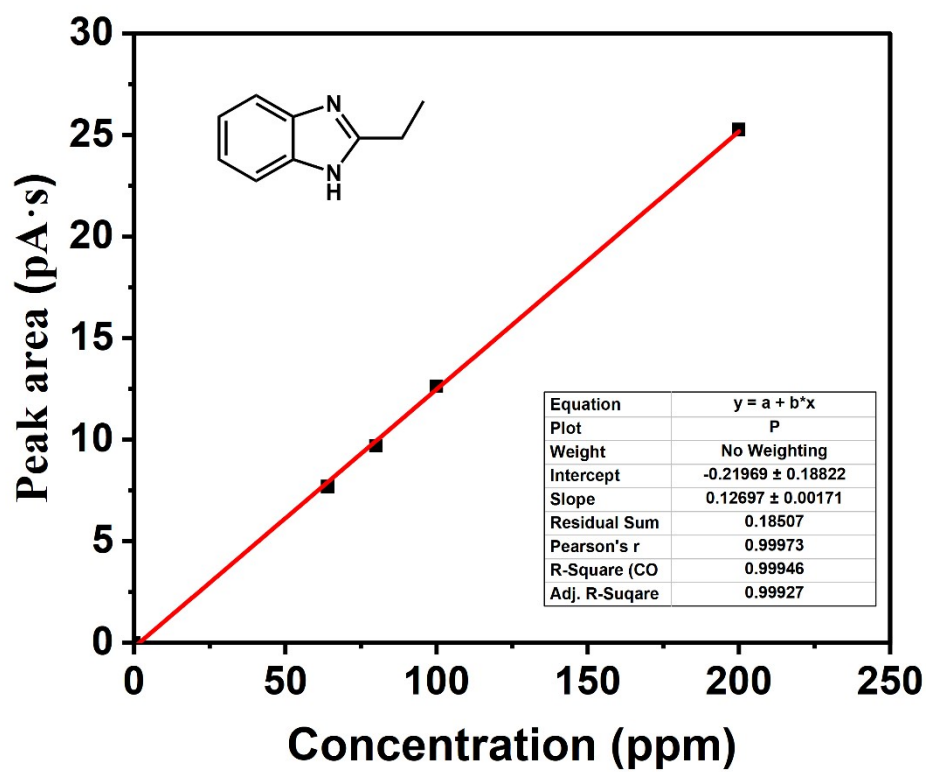


Figure S48. Standard curves of 2-ethylbenzimidazole by GC analysis.

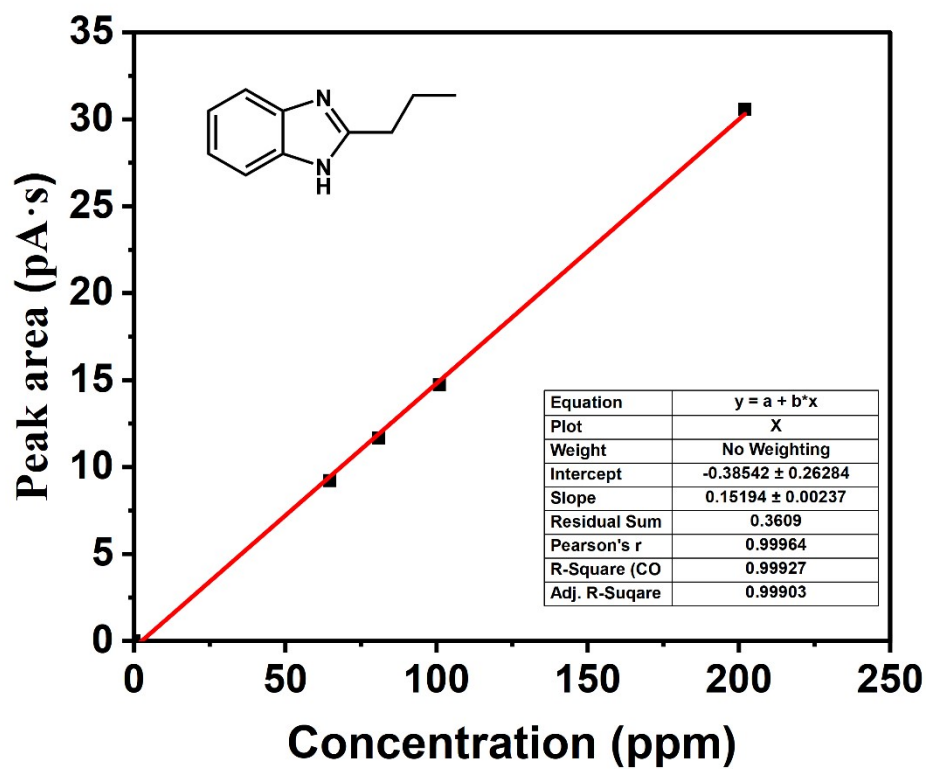


Figure S49. Standard curves of 2-propylbenzimidazole by GC analysis.

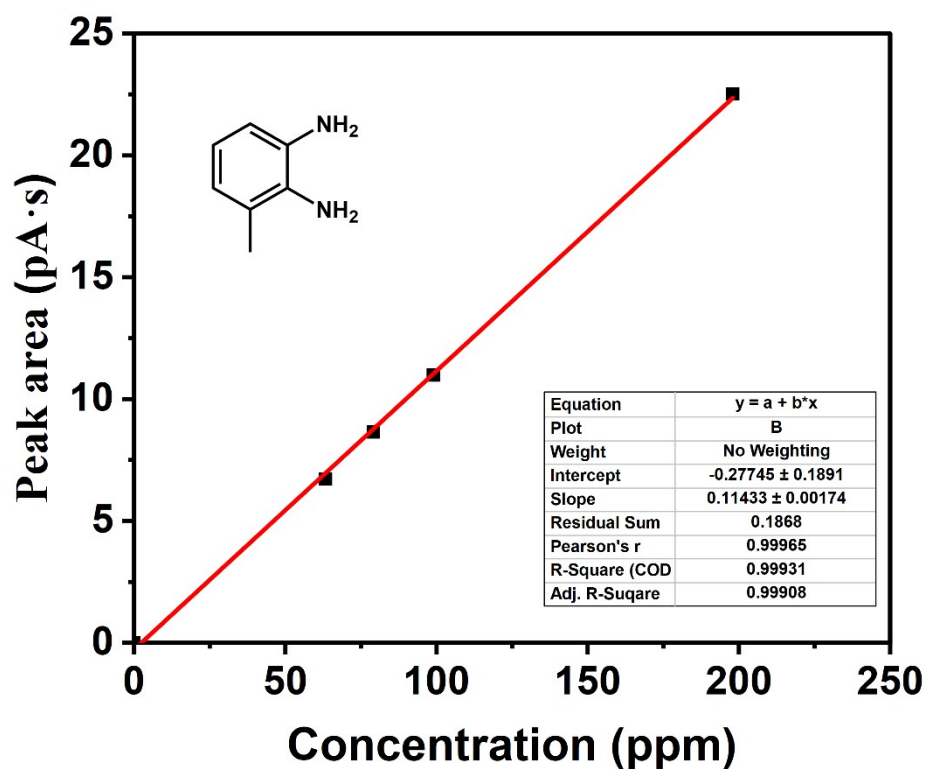


Figure S50. Standard curves of 2,3-diaminotoluene by GC analysis.

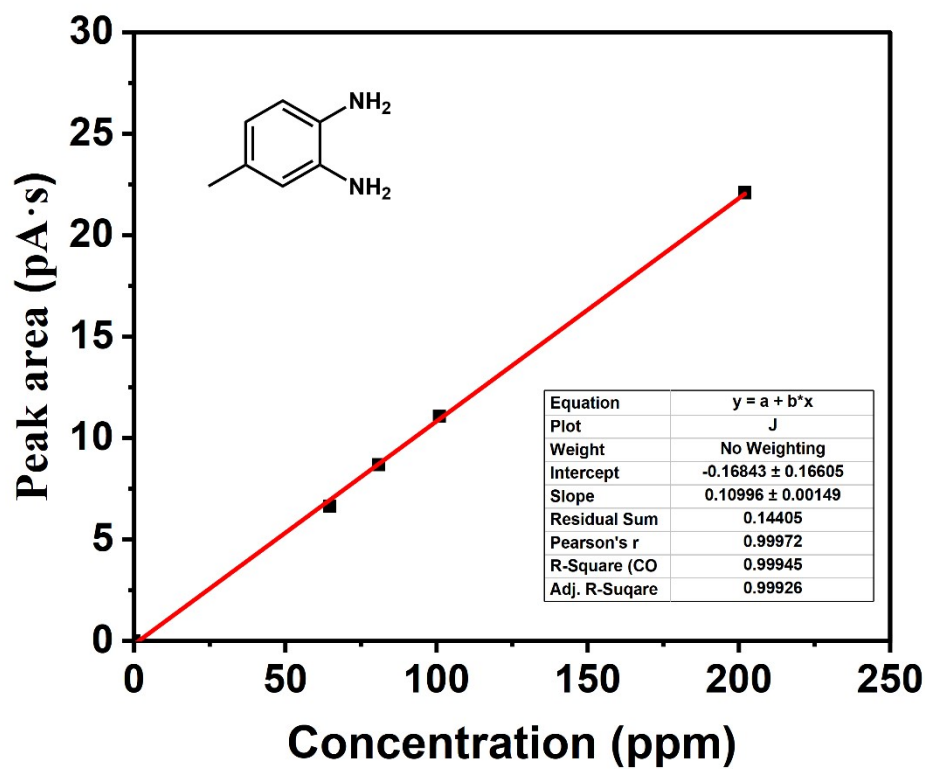


Figure S51. Standard curves of 3,4-diaminotoluene by GC analysis.

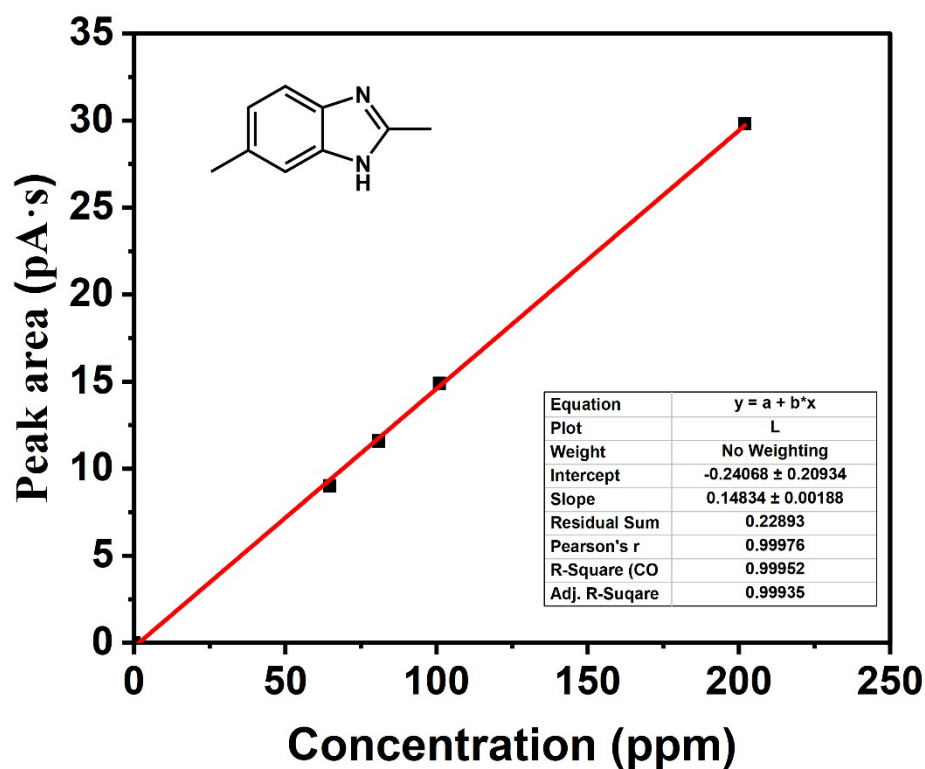


Figure S52. Standard curves of 2,5-dimethyl-1H-benzo[D]imidazole by GC analysis.

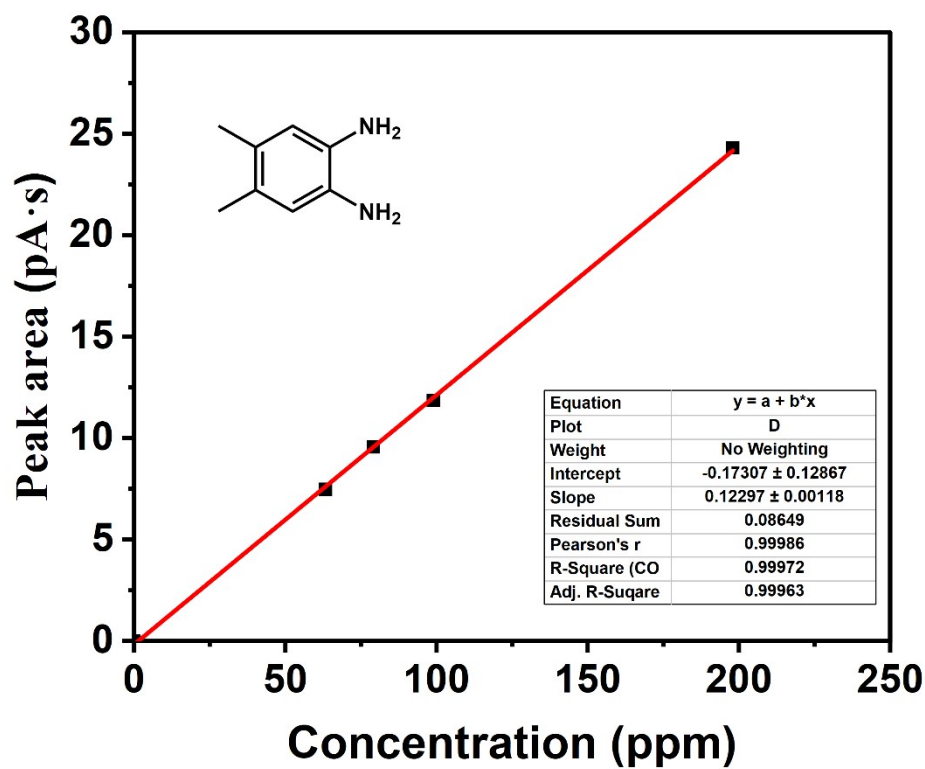


Figure S53. Standard curves of 4,5-dimethyl-1,2-phenylenediamine by GC analysis.

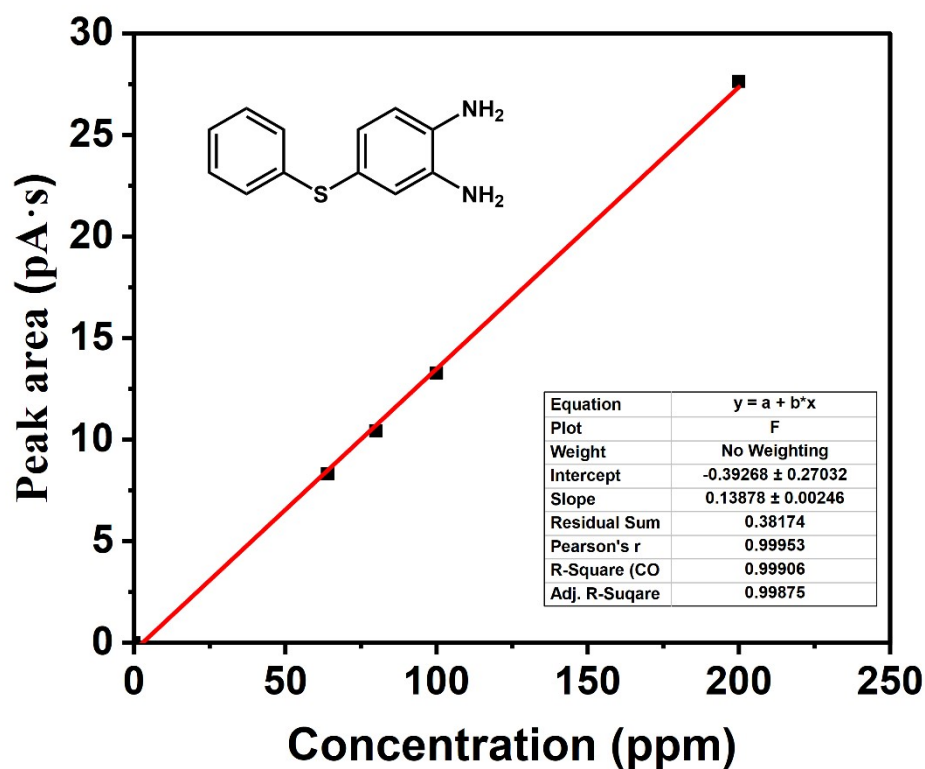


Figure S54. Standard curves of 4-(phenylthio)-1,2-benzenediamine by GC analysis.

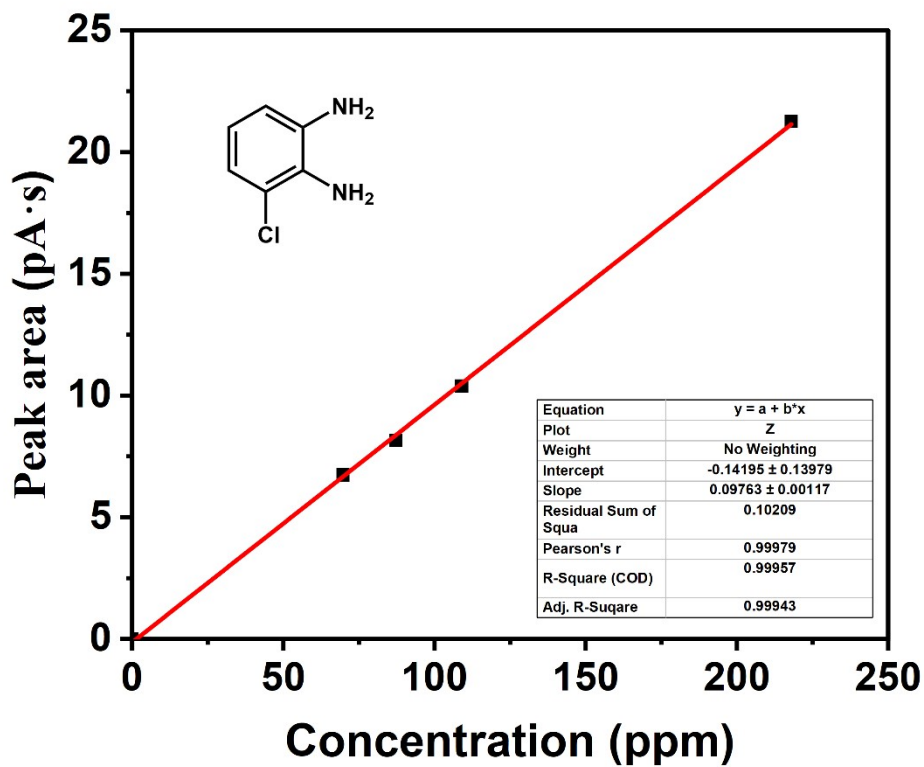


Figure S55. Standard curves of 3-chloro-1,2-phenylenediamine by GC analysis.

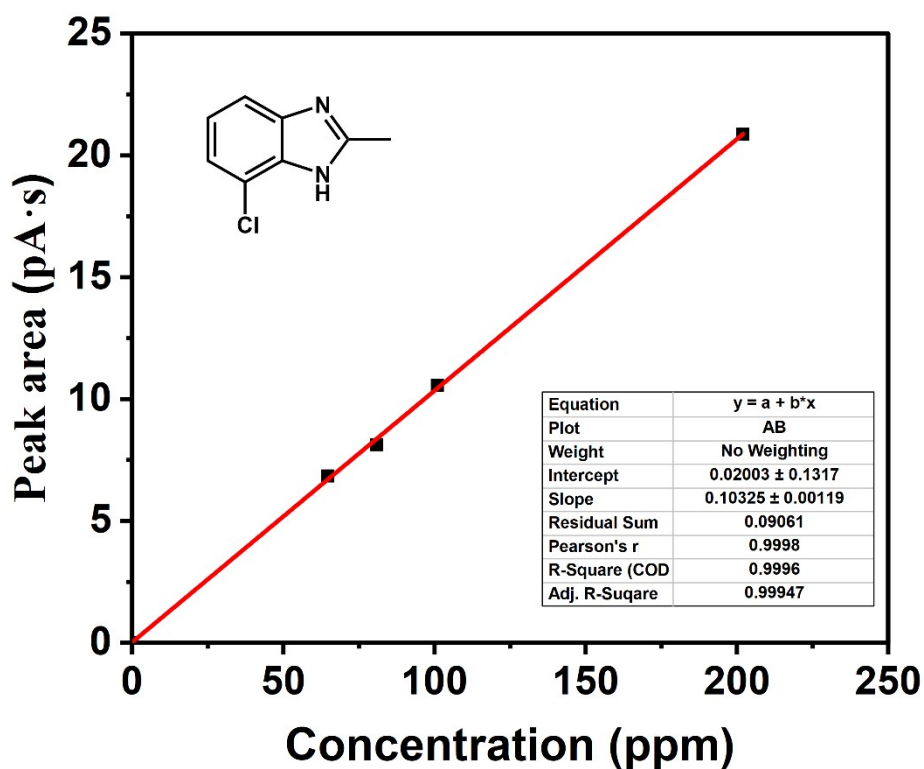


Figure S56. Standard curves of 4-chloro-2-methyl-1H-benzo[D]imidazole by GC analysis.

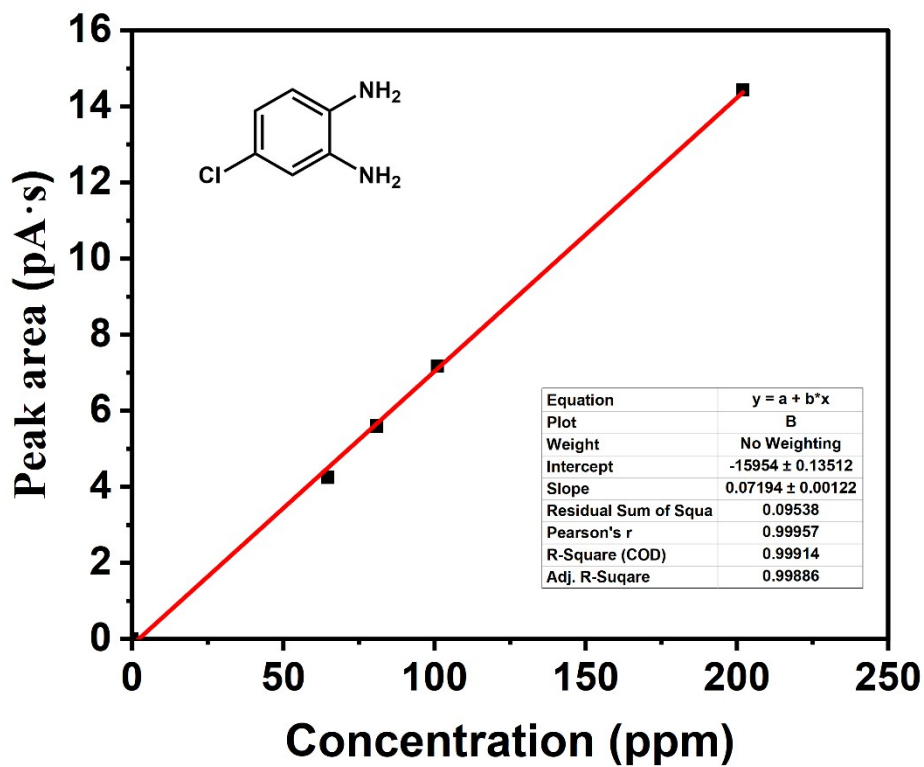


Figure S57. Standard curves of 4-chloro-1,2-diaminobenzene by GC analysis.

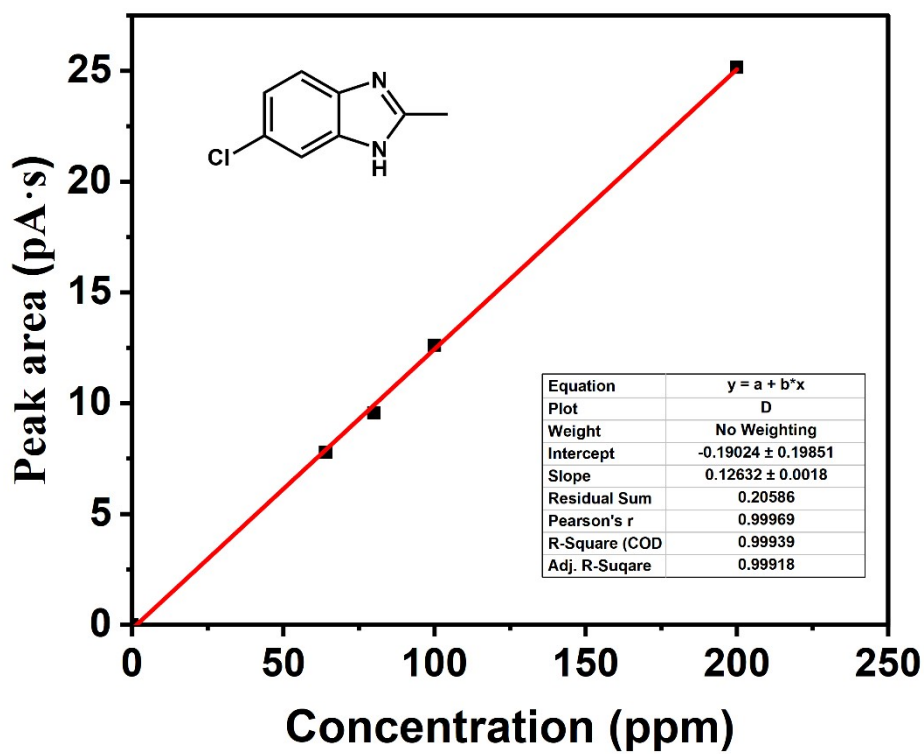


Figure S58. Standard curves of 5-chloro-2-methyl-1H-benzo[D]Imidazole by GC analysis.

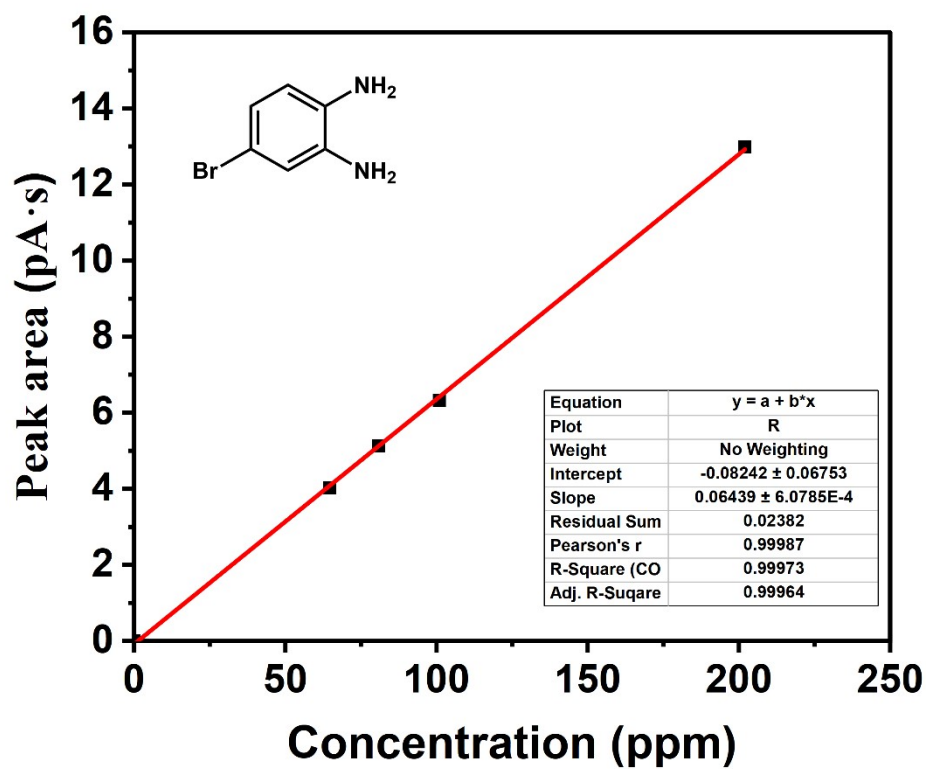


Figure S59. Standard curves of 1,2-diamino-4-bromobenzene by GC analysis.

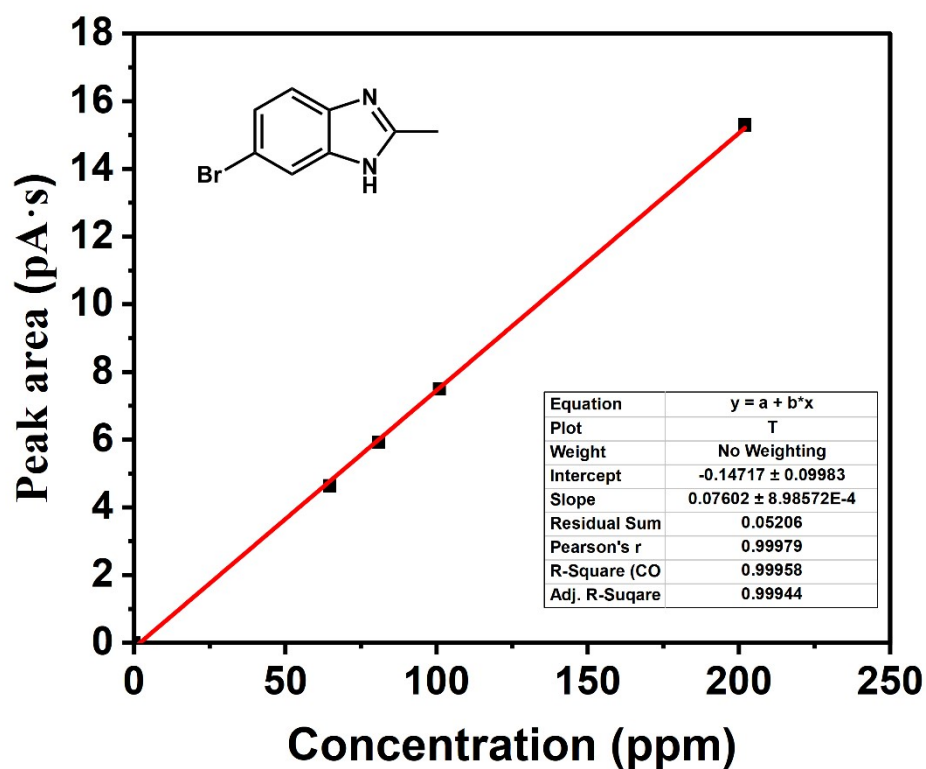


Figure S60. Standard curves of 5-bromo-2-methyl-1H-benzimidazole by GC analysis.

Reference

- [1] Hutter, J.; Iannuzzi, M.; Schiffmann, F.; VandeVondele, J., CP2K: atomistic simulations of condensed matter systems. *Wiley Interdisciplinary Reviews-Computational Molecular Science* 2014, **4** (1), 15-25.
- [2] Lippert, G.; Hutter, J.; Parrinello, M., A hybrid Gaussian and plane wave density functional scheme. *Mol. Phys.* 1997, **92** (3), 477-487.
- [3] VandeVondele, J.; Krack, M.; Mohamed, F.; Parrinello, M.; Chassaing, T.; Hutter, J., QUICKSTEP: Fast and accurate density functional calculations using a mixed Gaussian and plane waves approach. *Comput. Phys. Commun.* 2005, **167** (2), 103-128.
- [4] VandeVondele, J.; Hutter, J., Gaussian basis sets for accurate calculations on molecular systems in gas and condensed phases. *J. Chem. Phys.* 2007, **127** (11).
- [5] Goedecker, S.; Teter, M.; Hutter, J., Separable dual-space Gaussian pseudopotentials. *Phys. Rev. B* 1996, **54** (3), 1703-1710.
- [6] Perdew, J. P.; Burke, K.; Ernzerhof, M., Generalized Gradient Approximation Made Simple. *Phys. Rev. Lett.* 1996, **77** (18), 3865-3868.
- [7] Hapala, P.; Kichin, G.; Wagner, C.; Tautz, F. S.; Temirov, R.; Jelínek, P., Mechanism of high-resolution STM/AFM imaging with functionalized tips. *Phys. Rev. B* 2014, **90** (8), 085421.
- [8] Qin, Y.; Hao, M.; Xu, C.; Li, Z., Visible light initiated oxidative coupling of alcohols and *o*-phenylenediamines to synthesize benzimidazoles over MIL-101(Fe) promoted by plasmonic Au. *Green Chem.* 2021, **23** (11), 4161-4169.
- [9] Qin, Y.; Hao, M.; Ding, Z.; Li, Z., Pt@MIL-101(Fe) for efficient visible light initiated coproduction of benzimidazoles and hydrogen from the reaction between *o*-Phenylenediamines and alcohols. *J. Catal.* 2022, **410**, 156-163.
- [10] Huang, Z.-S.; Wang, Y.-F.; Qi, M.-Y.; Conte, M.; Tang, Z.-R.; Xu, Y.-J., Interface Synergy of Exposed Oxygen Vacancy and Pd Lewis Acid Sites Enabling Superior Cooperative Photoredox Synthesis. *Angew. Chem. Int. Ed.* 2024, e202412707.
- [11] Shiraishi, Y.; Sugano, Y.; Tanaka, S.; Hirai, T., One-Pot Synthesis of Benzimidazoles by Simultaneous Photocatalytic and Catalytic Reactions on Pt@TiO₂ Nanoparticles. *Angew. Chem. Int. Ed.* 2010, **49** (9), 1656-1660.
- [12] Wang, Y. F.; Qi, M. Y.; Conte, M.; Tang, Z. R.; Xu, Y. J., New Radical Route and Insight for the Highly Efficient Synthesis of Benzimidazoles Integrated with Hydrogen Evolution. *Angew. Chem. Int. Ed.* 2023, **62** (29), e202304306
- [13] Li, Z.; Ye, Z.; Chen, L.; Cui, J.; Chen, J., Hierarchically Nanoporous Titanium-Based Coordination Polymers for Photocatalytic Synthesis of Benzimidazole. *ACS Appl. Nano Mater.* 2020, **3** (11), 10720-10731.